Femtosecond X-ray Spectroscopy Directly Quantifies Transient Excited State Mixed Valency and Subsequent Vibronic Dynamics

Chelsea Liekhus-Schmaltz,[*,†] Zachary W. Fox,[†] Amity Andersen,[‡] Kasper S. Kjaer,[¶,§] Roberto Alonso-Mori,[‖] Elisa Biasin,[¶] Julia Carlstad,[⊥] Matthieu Chollet,[‖] James D. Gaynor,[⊥] James M. Glownia,[‖] Kiryong Hong,[#] Thomas Kroll,[@] Jae Hyuk Lee,[△,▽] Benjamin I. Poulter,[†] Marco Reinhard,[¶] Dimosthenis Sokaras,[@] Yu Zhang,[††,‡‡] Gilles Doumy,[¶¶] Anne Marie March,[¶¶] Stephen H. Southworth,[¶¶] Shaul Mukamel,[††] Amy Cordones-Hahn,[¶] Robert W. Schoenlein,[¶,‖] Niranjan Govind,[*,§§] and Munira Khalil[*,†]

[†]*Department of Chemistry, University of Washington, Seattle, WA, USA*

[‡]*Environmental Molecular Sciences Laboratory, Pacific Northwest National Laboratory, Richland, Washington 99352, USA*

[¶]*Stanford PULSE Institute, SLAC National Accelerator Laboratory, Menlo Park, CA 94025, USA*

[§]*Technical University of Denmark, Department of Physics, Fysikvej 307, DK-2800 Kongens Lyngby, Denmark*

[‖]*LCLS, SLAC National Accelerator Laboratory, Menlo Park, CA 94025, USA*

[⊥]*College of Chemistry, University of California, Berkeley, CA 94720, USA*

[#]*Gas Metrology Group, Korea Research Institute of Standards and Science, Daejeon*

34113, Republic of Korea

@SSRL, SLAC National Accelerator Laboratory, Menlo Park, CA 94025, USA

△Ultrafast X-ray Science Laboratory, Chemical Sciences Division, Lawrence Berkeley National Laboratory, Berkeley, CA 94820, USA

▽Pohang Accelerator Laboratory, Pohang, 37673, Republic of Korea

††Department of Chemistry and Physics & Astronomy, University of California, Irvine, CA 92697, USA

‡‡Q-Chem Inc., 6601 Owens Dr, Pleasanton, CA 94588, USA

¶¶Chemical Sciences and Engineering Division, Argonne National Laboratory, Lemont, IL, 60439, USA

§§Physical and Computational Sciences Directorate, Pacific Northwest National Laboratory, Richland, WA, 99352, USA

E-mail: cliekhus@uw.edu; niri.govind@pnnl.gov; mkhalil@uw.edu

Abstract

Quantifying charge delocalization and coupled nuclear motions on short-lived photoexcited states in solution remains experimentally challenging, requiring element specific femtosecond experimental probes of time-evolving electron transfer. Here, we use advanced X-ray spectroscopic probes and excited state calculations to measure the hole charge on the photoexcited charge transfer state of a prototypical mixed valence bimetallic ($Fe^{II}Ru^{III}$) complex in water. We find that the hole charge at the Fe atom is 0.75 ± 0.18 on the metal-to-metal charge transfer excited state, which has a 58 ± 10 fs lifetime. The X-ray emission data reveals that the rapid back electron transfer excites vibrations that modulate the Fe-Ru distance on the non-equilibrium ground state. Our combined experimental and computational approach provides a spectroscopic ruler to quantify excited state valency and sheds light on the low-frequency nuclear vibrations that are coupled to core level transitions.

1   Introduction

Understanding and ultimately controlling charge flow within a molecule is a key requirement for the targeted synthesis of efficient artificial light harvesters and photochemical energy converters.[1,2] Critical to achieving this goal is measuring nuclear and electronic motion on short-lived excited states and a non-equilibrium ground state as the molecule undergoes photoinduced electron transfer. Cyanide-bridged transition metal mixed valence compounds serve as excellent model systems to probe the coupling between electronic and vibrational (vibronic) motions during ultrafast photoinduced electron transfer reactions. These complexes contain oxidizing and reducing moieties, making them widely studied for their applications in photomagnetism and photochemical energy conversion. Time-resolved optical spectroscopy, infrared (IR) and 2D spectroscopies have made important measurements of ultrafast charge transfer in mixed valence systems by measuring relevant solvent-dependent kinetic parameters of electron transfer and identifying the role of the coupled high-frequency cyanide vibrations in the photoinduced forward and back electron transfer processes.[3–10] These ultrafast studies have shown that two properties play key roles in electron transport: vibronic coupling and electron delocalization.[5,11–14] Both properties control the dispersal of energy during electron transfer and ultimately determine the geometric and electronic changes during excitation and relaxation.

Electron delocalization has largely been studied under the Robin-Day classification system which attributes the extent of delocalization to electronic coupling between two metal centers: Class I (uncoupled, localized charges), Class II (moderately coupled), Class III (strongly coupled, delocalized charges).[15] The Robin-Day classification is based on IR and near IR spectroscopy, which are indirect indicators of the valence charge distribution, making direct determinations of electron delocalization between the transition metal centers a challenging problem. Furthermore, ultrafast optical and IR studies are fundamentally limited in their ability to simultaneously spatially and temporally resolve the non-equilibrium electronic dynamics involved in photocatalytic molecular complexes. The lack of direct ex-

perimental measurements of electronic character makes quantitative connection to theory difficult, which has resulted in a significant knowledge gap for developing predictive design principles to harness molecular energy capture or electron transfer in chromophore-catalyst assemblies. In contrast to optical and IR studies, X-ray absorption and X-ray emission spectroscopies (XAS and XES) probe transitions with core level atomic orbitals, making them selective and sensitive to local atomic and electronic changes.[16] In addition, a high resolution XAS technique, high energy resolution fluorescence - X-ray absorption near edge spectroscopy (HERFD-XANES), can be used to monitor small spectral changes in absorption by detecting fluorescence X-ray photons emitted through a longer lived intermediate state resulting in reduced spectral broadening and a high resolution spectrum.[17–23] Recent advancements at X-ray Free Electron Lasers (XFELs), such as at the Linac Coherent Light Source (LCLS), enable the production of high-intensity, tunable, < 45 fs X-ray pulses for ultrafast XES and HERFD-XANES measurements of atomic and electronic structural dynamics of dilute solution samples.[24,25] These time resolved X-ray studies have successfully monitored solvation dynamics such as spin crossovers, nuclear oscillations, and charge migration in solvated metal ligand complexes.[26–36]

In this study, we extend ultrafast XES and HERFD-XANES measurements to study electron transport between the two metal centers in a solvated mixed valence complex. The mixed valence transition metal complex we investigate is $[(CN)_5Fe^{II}CNRu^{III}(NH_3)_5]^-$, FeRu for brevity, which has a metal-to-metal charge transfer (MMCT) transition in the near-IR region of the UV-Vis spectra, shown in Fig. S2 of the Supplementary Information along with its transition density in Fig. S3. Its properties have been been studied extensively optically and in particular 2D vibrational-electronic spectroscopy shows that the cyanide bridge stretching mode is strongly coupled to the MMCT transition and becomes excited following the electronic excitation.[4,9,37–39] Transient optical experiments have reported an ultrafast back electron transfer (BET) time of 89 ± 10 fs,[3] implying that ultrafast and spatially localized measurements are necessary for characterizing the BET. Additionally, a

4

recent ultrafast X-ray scattering experiment demonstrated how coherent solvent motions play an important role in the BET dynamics.[40] Missing from these experiments is a measure of the MMCT state valency and a direct measure of the coupled electronic and nuclear motion during the BET. These characteristics make FeRu an ideal system for studying electron transfer dynamics in a mixed valence system.

Here, we report time-resolved Fe K-edge XES and Fe K-edge HERFD-XANES measurements of aqueous FeRu after excitation to a MMCT state in order to capture its ultrafast BET (< 100 fs), and characterize the electron transfer and the accompanied non-equilibrium nuclear motion. We show that time-resolved XES is sensitive to both electron transfer as well as low frequency vibrational motion and that time-resolved HERFD-XANES can probe the electron density and therefore the degree of electron delocalization around the Fe atom. By combining our measurements with ground and excited state calculations including explicit solvation, we measure the mixed valency of an excited state species and monitor nuclear motion that occurs after electron transport.

2 Results and Discussion

2.1 Kα_1 XES Kinetic Traces Yield the BET Time

We begin our analysis by examining the dynamics of the MMCT and BET in FeRu with the time resolved XES measurement. The experimental setup for this measurement is shown in Fig. 1, along with the relevant molecular orbitals. Time dependent Kα_1 (2p$_{3/2}$ to 1s) X-ray emission spectra were measured with the Rowland spectrometer as a function of the pump probe delay. The percent change in the X-ray emission taken at 6402.7, 6401.2, and 6404.1 eV as a function of probe probe delay is shown in Fig. 2. The equation defining the energy and time dependent X-ray emission spectra is given by Eq. 2 in the Supplementary Information, and the uncertainty associated with each time point is determined by bootstrapping, discussed in Section 3.4 of the Supplementary Information. We see that the emission peak

decreases, while the low-energy portion of the emission spectra immediately increases in intensity after the MMCT. After several 100s of fs, the system returns to the ground state spectra.
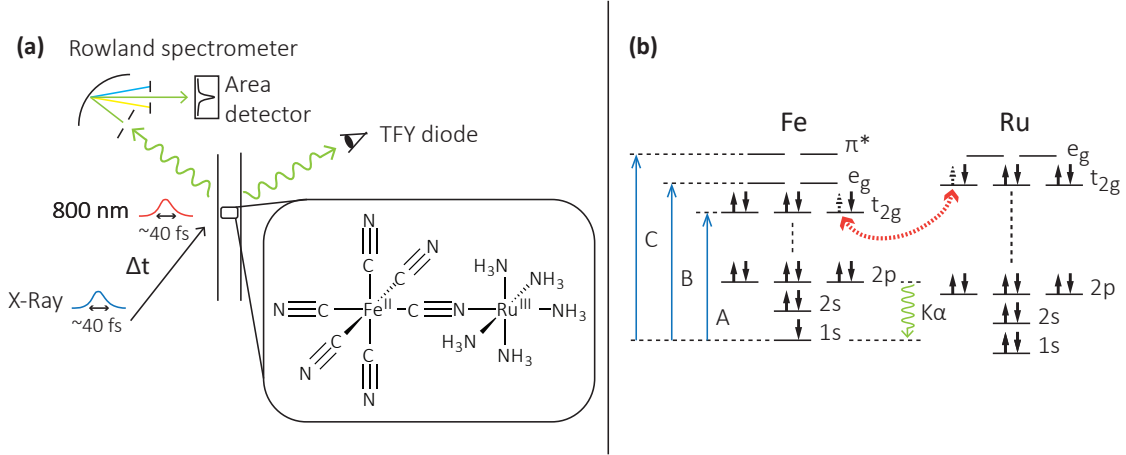

Figure 1: **Experimental Setup.** Our experiment was performed at the X-ray Pump Probe endstation at LCLS, shown in (a). The sample, FeRu, was dissolved in water and introduced to a Helium filled chamber via a liquid jet. We used an 800 nm, 40 fs FWHM long, optical pulse to induce a MMCT transition in FeRu and then monitor the resulting dynamics with a 40 fs FWHM long Fe K-edge X-ray pulse. The relevant atomic and molecular orbitals are shown in (b). The optical excitation and resulting BET is shown as the red dashed line. An above edge X-ray probe is used for XES measurements, in order to remove a 1s electron resulting in $K\alpha_1$ emission, shown by the green wavy arrow, which is a $2p_{3/2}$ to 1s transition. A below edge X-ray probe, shown as blue arrows, is used for the time-resolved HERFD-XANES measurements. The HERFD-XANES probe is scanned over the 1s to t_{2g}, e_g, and $\pi*$ orbitals which we label the A, B, and C peaks, respectively.

By comparing our measured FeRu spectra to the model complexes ($[Fe^{II}(CN)_6]^{4-}$) and ($[Fe^{III}(CN)_6]^{3-}$) discussed in the Section 4.2, we can evaluate how the Fe oxidation state of FeRu affects its emission spectrum. The ground state emission spectra of the model complexes are displayed in the inset of Fig. 2. The emission spectrum of ($[Fe^{III}(CN)_6]^{3-}$) is both broadened and blue shifted relative to ($[Fe^{II}(CN)_6]^{4-}$). This is due to an increase in the effective charge of the Fe atom and an increase in the exchange interaction between the 2p electrons and the higher spin 3d electrons.[41] The resulting percent difference XES spectrum between ($[Fe^{II}(CN)_6]^{4-}$) and ($[Fe^{III}(CN)_6]^{3-}$) has a characteristic dispersive profile with a peak at 6402 eV and a minimum at 6404 eV. These energy regions are therefore markers of the Fe

atom oxidation state.

The main portion of Fig. 2 shows that the percent difference FeRu XES spectra changes are consistent with the changes in Fe oxidation state of the model complexes. Figure S7 in the Supplementary Information shows the full spectral difference of the excited state, which while noisy, is also consistent with the changes in XES between the oxidation states. We conclude that the FeRu time dependent XES is characteristic of the Fe atom in FeRu changing from having Fe^{II} character in the ground state to having more Fe^{III} character in the excited state.

To interpret the dynamics in the time dependent XES signal we represent the time dependent XES traces with a double exponential fit. We were able to fit the dynamics with a two electronic state model (the ground state and the MMCT state), and measure the BET to be 58 ± 10 fs, with a second decay time of 510 ± 120 fs which only has significant amplitude in the 6404.1 eV kinetic trace. This is likely due to the fact that the 6404.1 eV emission line has the best signal to noise, as seen in the error bars in Fig. 2. The corresponding instrument response function (IRF) given by the FWHM is 86 ± 7 fs. We use the measured amplitudes in conjunction with the model complexes' spectra to compute an excitation fraction of $20 \pm 5\%$. Consistent BET and IRF times as well as excitation fraction are found for the time-dependent Kβ emission spectra also collected at this experiment, which is discussed in Ref. 40. The uncertainties we report are given by the fit covariance matrix. All of the fitting parameters are shown in Table S6 of the Supplementary Information.

The time scales measured above are consistent with an 89 ± 10 fs BET and a longer 1900 $\pm$ 1200 fs decay measured in Ref. 3. Given that Ref. 3 used transient optical absorption measurements which necessarily contain many overlapping spectral components, it is consistent that their observed electronic lifetime is broadened compared to time resolved XES which is a more sensitive probe of the Fe oxidation state. We associate the shorter time decay with the BET and the longer time delay with vibrational cooling on the ground state following the BET. Previous time resolved optical experiments similarly show that the BET results
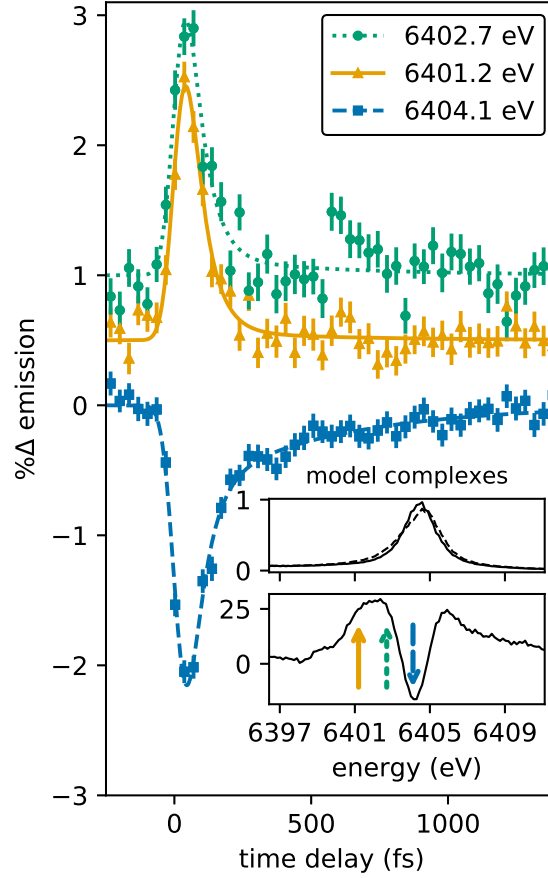
Figure 2: **Time-resolved difference XES spectra.** In the main figure we monitor the Kα₁ X-ray emission of FeRu as a function of pump probe delay at the three energies shown in the legend and in the inset. Each kinetic trace is offset by 0.5% to improve visibility. The uncertainty of each point is determined by bootstrapping. We use a global fit to determine a BET of 58 ± 10 fs, an IRF of 86 ± 7 fs, and a second, longer decay of 510 ± 120 fs. Also visible are oscillations on top of the decay. Their corresponding frequencies are shown in Fig. 3 and S8. The ground state Kα₁ emission of the aqueous model complexes (($[\mathrm{Fe^{II}(CN)_6}]^{4-}$) as the solid line and ($[\mathrm{Fe^{III}(CN)_6}]^{3-}$) as the dashed curve) is shown in the upper panel of the inset. The percent change between the two complexes is shown in the lower panel.

in a vibrationally hot ground electronic state.[3,4] We conclude that the MMCT initiates an ultrafast population transfer from the MMCT state to the ground state which results in a vibrationaly hot ground state.

2.2 XES Fourier Analysis Reveal Coupled Low Frequency Modes

In addition to the overall decay observed in the XES signal, we also find small superimposed oscillations that are strongest for the 6404.1 eV emission line, as seen in Figs. 2 and 3. Traditionally XES has been unable to definitively resolve nuclear oscillations, however, recent time-resolved XES measurements of iron carbene show that coherent nuclear motion on long lived excited states initiated by a charge transfer transition can shift the $K\alpha$ and $K\beta$ emission spectra, manifesting in oscillations in emission line intensities.[33,42] We will show that the oscillations we observe in our XES spectra occur on the ground electronic state following the BET and can be used to observe low frequency nuclear motion.

Fourier transforms of the oscillations shown in Fig. S8 of the Supplementary Information show that there are two frequency components in the oscillation. To isolate them we fit the residuals of the exponential decay with a delayed onset double cosine function smoothed by the IRF. The cosine fit added to the exponential fit is shown in Fig. 3 and the fitting parameters are shown in Table S8 of the Supplementary Information. The two oscillations have periods 300 ± 10 fs and 148 ± 4 fs with corresponding frequencies of 109 ± 6 cm^{-1} and 220 ± 10 cm^{-1} and an offset delay of 110 ± 16 fs.

Similar oscillations could be induced by an impulsive Raman transition since the duration of our excitation pulse is shorter than both oscillations, however we expect impulsive Raman oscillations to begin immediately at time zero.[43,44] Impulsive Stimulated Raman Scattering (RISRS) has been observed in a similar ruthenium dimer complexes when excited with a 795 nm, < 20 fs pulse, initiating low frequency oscillations of 100 to 200 cm^{-1} that begin at time zero.[3] However the same paper does not observe any low frequency RISRS oscillations in FeRu, which is excited under the same conditions. In contrast, the oscillations observed
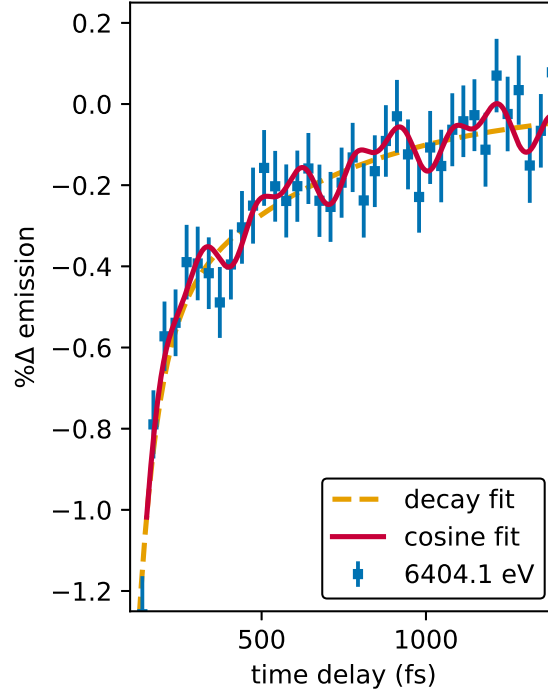
Figure 3: **XES oscillation fits.** The double cosine fit is added to the exponential fit and plotted in red. The measured time-dependent XES signal is shown with blue squares, with the BET fit in Eq. 3 shown as the yellow dashed curve. The two oscillations have periods of 300 ± 10 fs and 148 ± 4 fs and an offset delay of 110 ± 16 fs.

here appear with a time delay of 110 fs, which is indicative of a nuclear wavepacket returning to the ground electronic state after the BET.

These oscillations indicate that low frequency modes constitute some portion of the vibrational states in the vibrationally hot ground state identified in the previous section. Reference 40 similarly found low frequency oscillations and onset time arising from solvent dynamics with a frequency of about 180 cm^{-1}. This oscillation is similar to the higher frequency we observe here, so we consider the possibility that the solvent could affect the emission spectra. While it is unlikely that Kα_1 emission would be directly sensitive to solvent motion, the solvent could affect the electron density around the Fe atom, and we cannot directly rule this possibility out. However, given that the solvent oscillations cannot account for the lower frequency oscillations at 110 cm^{-1}, we consider the other possibility that the oscillations are due to intramolecular motion. To estimate how such nuclear motion can affect Kα_1 emission of FeRu, we calculated the 1s-2p$_{3/2}$ energy splitting over the course of a ground state QM/MM molecular dynamics trajectory. We found that low frequency modes can shift the Kα_1 emission spectra by up to 0.1 eV, as shown in Fig. S11 in the Supplementary Information. From the Fourier transform of the calculated time resolved 1s-2p$_{3/2}$ energy splitting we can estimate that the modes with frequencies less than 250 cm^{-1} can shift the emission energy by 0.03 eV. Figure S12 shows how we can use this estimated shift to give an expected oscillation amplitude of 0.3%. This amplitude estimate is on the same order as the amplitudes found for the two oscillations: 0.06 ± 0.02% and 0.1 ± 0.05% for the low and high frequency respectively.

To assign these frequencies to specific normal modes we performed a harmonic analysis to reveal several low frequency modes involving motion around the Fe atom. For example, a 174 cm^{-1} mode that involves the Fe and Ru atoms oscillating relative to one another in a breathing mode is shown Fig. 4 and involves a change in Fe-Ru distance of 0.2 Å. Previous 2D vibrational-electronic spectroscopy revealed that the cyanide bridge is strongly coupled to the BET, and it is therefore consistent that the 174 cm^{-1} mode, which involves

motion along the bridge, would also be excited.[4,5] Additional possible modes are shown in the Supplementary Information in Fig. S9 with the corresponding ground state IR spectra in Fig. S10. Given the anharmonicity associated with such low frequency modes and that we know from Section 2.1 that the molecule is in a hot vibrational state, it is difficult to directly assign the measured Fourier components to any specific calculated mode since they are ground vibrational state calculations. Instead, we conclude that several low frequency modes are excited after the MMCT and that these low frequency modes can couple to the core orbitals of the Fe atom. Combining this observation with the dynamics seen in the kinetic trace and the longer decay time associated with vibrational cooling, we conclude that these vibrations are a result of the molecular wavepacket returning to the ground state after the BET.
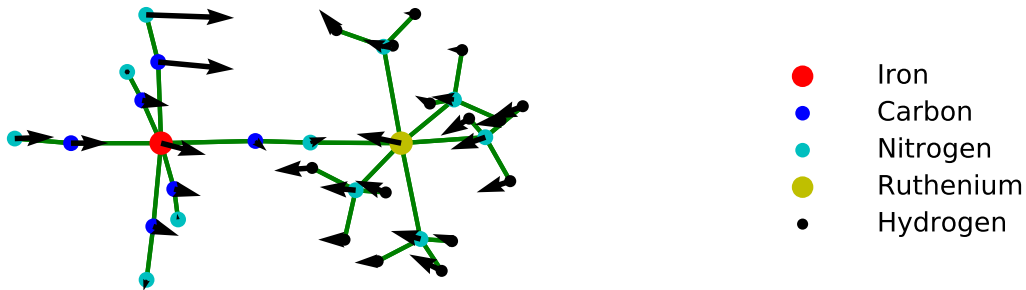
Figure 4: **Harmonic mode vectors for 174 cm^{-1}.** The harmonic mode vector for the 174 cm^{-1} mode is shown. It directly involves the Fe atom which makes it a likely candidate for the low frequency modes identified through time resolved XES. It involves a breathing mode between the Fe and Ru atoms.

2.3 Time-Resolved HERFD-XANES Probes Electron Hole Charge

Examining the time dynamics of the MMCT and BET in the previous section showed that the BET involves two electronic states with different Fe oxidation states that relax to a hot vibrational state. In this section we report the HERFD-XANES measurements of FeRu immediately upon MMCT to examine the electronic structure of the excited state and measure its mixed valency. As with the time dependent XES measurement, we use the Rowland spectrometer tuned to the peak of the $K\alpha_1$ emission, as shown in Fig. 1, to measure the HERFD-XANES spectrum. While we measured both the transient HERFD-XANES and traditional XANES spectra from the TFY diode, the spectral changes we observe were only resolvable with the HERFD-XANES measurements. This is due to the smaller bandwidth of the HERFD-XANES spectra, an explanation for which is given in Fig. S5.

In Fig. 5 we present the HERFD-XANES spectrum of FeRu immediately upon the MMCT, with X-ray delays between -35 fs and 35 fs. This delay range was chosen to cover the initial excitation MMCT, which has a lifetime of 58 ± 10 fs. The time resolved HERFD-XANES spectrum is given in Eq. 5 of the Supplementary Information, and the uncertainty associated with each incident energy is determined by bootstrapping, which is discussed in Section 3.4 of the Supplementary Information. The ground state HERFD-XANES of FeRu spectra taken at LCLS is compared to the HERFD-XANES of the aqueous model complexes ($[Fe^{II}(CN)_6]^{4-}$) and ($[Fe^{III}(CN)_6]^{3-}$) taken at APS shown in the top panels of Fig. 5. These measurements are also compared to the ground state XANES calculation of FeRu in Fig. S13 of the Supplementary Information. The transient difference HERFD-XANES spectra between the excited and the ground state is shown in the bottom panels of Fig. 5.

The ground state FeRu HERFD-XANES spectrum shows two peaks, one at 7114 eV, labeled the B peak, and one at 7117 eV, labeled the C peak. While the HERFD-XANES spectrum is dependent on both the absorption strength at the incident energy and the $K\alpha_1$ emission strength, at the peak of the $K\alpha_1$ emission, the primary factor determining the HERFD-XANES intensity is the absorption at the incident energy rather than any off-
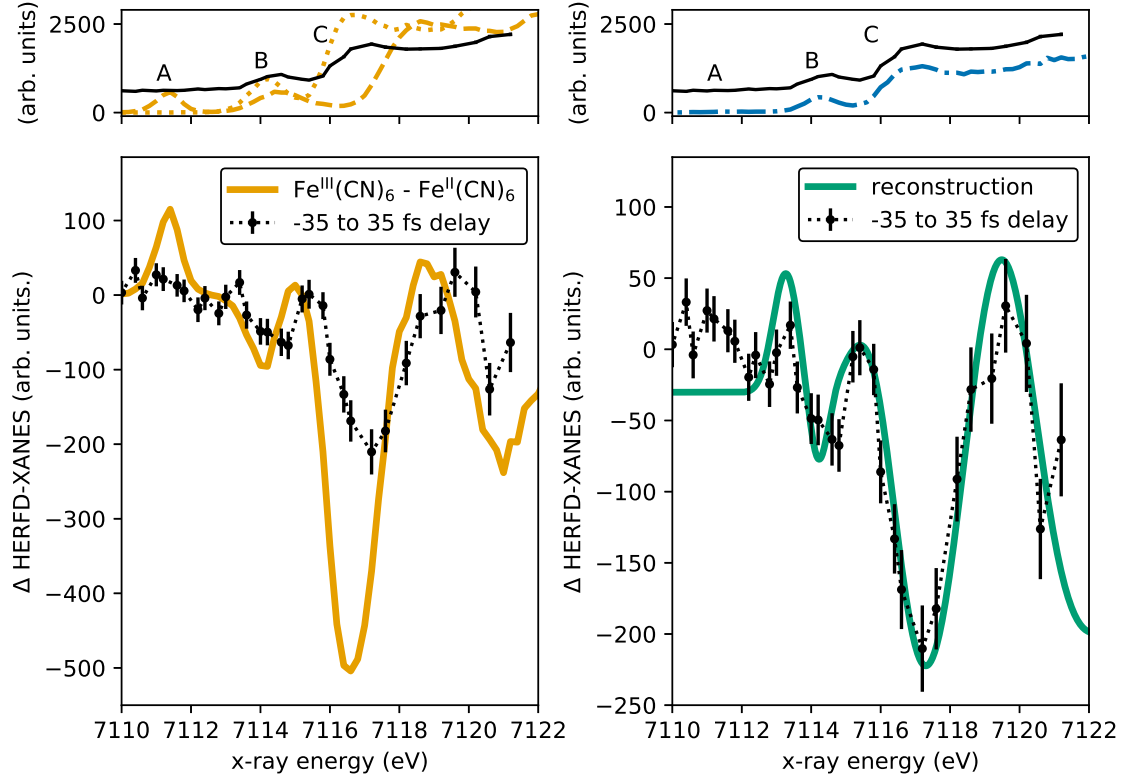
Figure 5: **Transient HERFD-XANES spectra.** The upper left panel shows the ground state HERFD-XANES spectra of FeRu taken at LCLS (black solid), ($[Fe^{II}(CN)_6]^{4-}$) taken at APS (yellow dotted), and ($[Fe^{III}(CN)_6]^{3-}$) taken at APS (yellow dashed). The upper right panel shows the ground state HERFD-XANES spectra of FeRu taken at LCLS (black solid) and the ground state HERFD-XANES spectra of FeRu taken at APS (blue dashed dotted). The APS signals are scaled by a common factor so that the APS FeRu B peak matches the amplitude of the LCLS FeRu B peak. Since the excited state FeRu HERFD-XANES spectra is measured at the peak of the ground state $K\alpha_1$ line, we also show the ($[Fe^{III}(CN)_6]^{3-}$) HERFD-XANES spectra at the peak of the ($[Fe^{II}(CN)_6]^{4-}$) $K\alpha_1$ line. The difference spectra between the excited and ground state FeRu spectra is shown as black circles in the lower panels. To measure the A, B, and C peaks positions, we reconstruct the difference spectra from the spectra in the above panels resulting in a measured A-B peak splitting of 2.5 ± 0.3 eV and a measured B-C peak splitting of 3.8 ± 0.3 eV. The final reconstruction is shown as a thick green line in the lower right panel, and details of its construction are discussed in Section 3.7 of the Supplementary Information. To compare, the difference between the two model complexes is show in the thick yellow line in the lower left panel.

diagonal peaks in the RIXS plane, therefore we can associate each peak with an absorption transition.[45] Peaks B and C shown in Fig. 1, correspond to an excitation of an electron from the 1s Fe atomic orbital to the e_g and π^* molecular orbitals, respectively. The transient difference spectrum shows dispersive line shapes after the MMCT in the B and C peak regions, which is due to the peaks blue shifting. A new peak labeled the A peak appears at 7113.3 eV and corresponds to an excitation from the 1s to t_{2g} molecular orbital, which is normally filled in the ground electronic state.

The observed change in the spectra is consistent with the spectral differences shown in the top left panel of Fig. 5 caused by an oxidation change between the two model complexes discussed in Section 4.2. Comparing the two complexes shows that the A peak is missing in $([Fe^{II}(CN)_6]^{4-})$ but visible in $([Fe^{III}(CN)_6]^{3-})$ where the t_{2g} orbital is unfilled. Additionally, the B and C peaks in $([Fe^{III}(CN)_6]^{3-})$ are blue shifted compared to $([Fe^{II}(CN)_6]^{4-})$ due to an increase in the effective charge on the Fe atom, increasing the ionization potential. A comparison of the transient difference HERFD-XANES spectra of FeRu and the difference spectra of the two model complexes in Fig. 5 shows that the excited state FeRu A peak is significantly less shifted than for $([Fe^{III}(CN)_6]^{3-})$. This suggests that the transient Fe atom oxidation state is less than the oxidation state difference between the two model complexes, which have a nominal oxidation state difference of one electron, and some delocalization of the electron hole on the Fe atom could be affecting the transient HERFD-XANES measurement.

To examine the delocalization, we calculate the hole charge on the Fe atom and Fe K-edge XANES on structures obtained along the MMCT excited state as described in Section 4.3. The importance of the solvation environment on the calculated XANES spectra was discussed in Refs. 46, 47 and 48 and our ground and excited state XANES calculations include explicit solute-solvent interactions. With our calculated spectra we can examine how the peak positions vary with the valency of the Fe atom by calculating its hole charge. To do so, we calculated the XANES spectra of the FeRu molecule on the excited state and associate the calculated spectra with the instantaneous Fe hole charge along the trajectory.
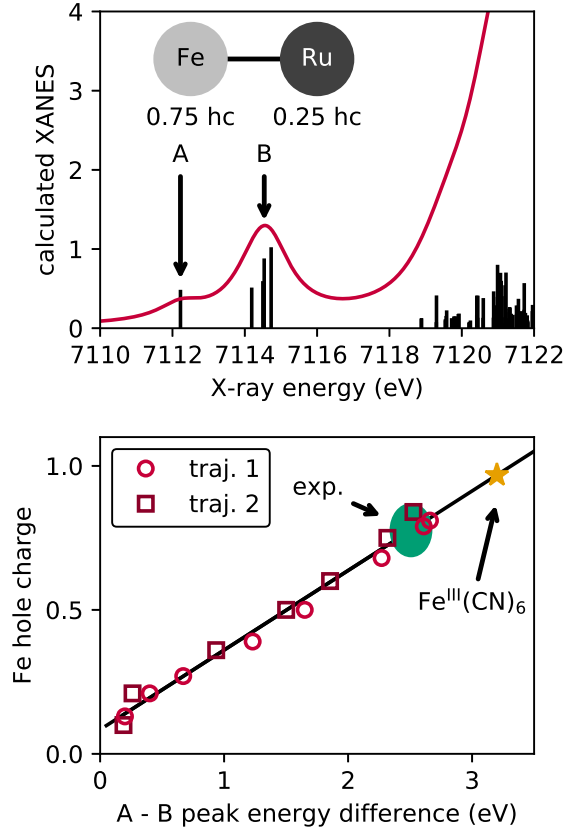
Figure 6: **Calculated and measured hole charge.** The lower panel shows the calculated Fe hole charge as a function of the A-B peak splitting. The corresponding experimental measurement is shown as the green oval with the uncertainty given by its size. For comparison, the splitting between the A and B peak for $([Fe^{III}(CN)_6]^{3-})$ is given by the yellow star. In the upper panel, the calculated spectra is shown for the integrated Fe hole charge closest to the measured value. The arrows indicate the positions of the calculated A and B peak.

For each hole charge, the calculated A peak energy is given by the lowest energy transition, and the position of the calculated B peak is given by the broadened B peak transitions. As shown in Fig. 6 the energy splitting between the A and B peak is nearly linear with the Fe hole charge which means the A-B peak energy splitting can be used as a new ruler for determining the Fe hole charge.

This trend can be understood by examining the excited state roots in Fig. S19 in the Supplementary Information. We see that while the A peak moves significantly with the hole charge, peak B is mostly stationary. An examination of the transition densities involved in the A and B peaks illuminates why this is true. The transition associated with the A peak is strongly localized on the Fe atom, making it a good probe of the localized electron density around the Fe atom, while the B peak is more delocalized throughout the molecule, as seen in Fig. 7. Molecular orbitals involved in the A, B, and C transitions are shown in Figs. S16, S17, and S18 of the Supplementary Information.

(a)   (b)

(c)   (d)
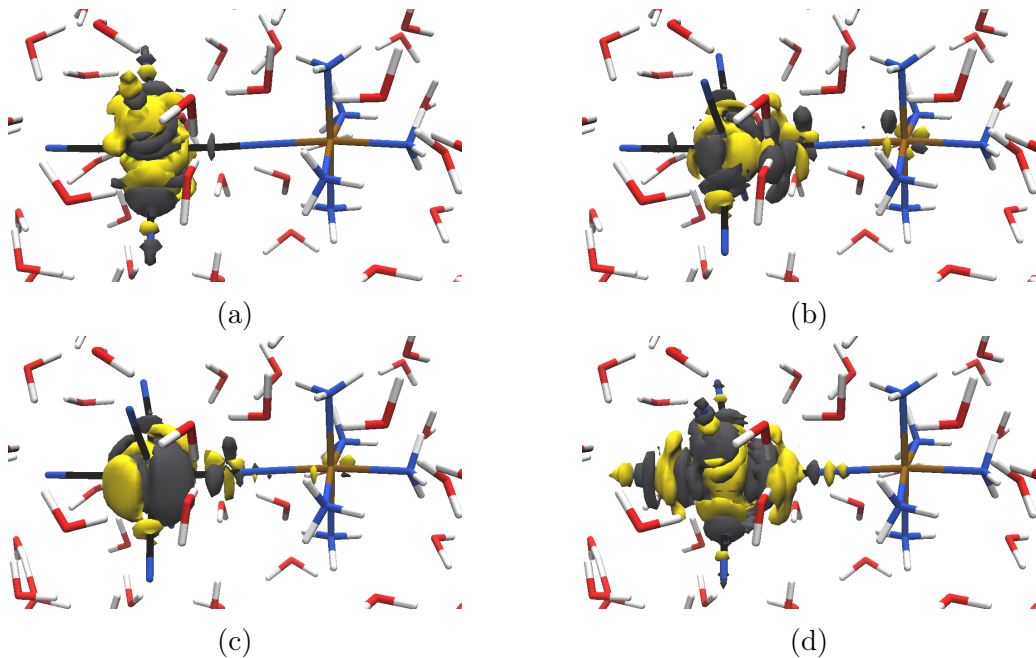
Figure 7: **Calculated A and B transition density plots.** The negative density is grey while the positive density is yellow. (a) A peak transition for a 0.1 Fe hole charge. (b) B peak transition for a 0.1 Fe hole charge. (c) A peak transition for a 0.68 Fe hole charge. (d) B peak transition for a 0.68 integrated Fe hole charge.

We will use the computed linear relationship between the hole charge on the Fe atom and the A-B splitting as a kind of molecular ruler to determine the experimental hole charge on the Fe atom after the MMCT. To do so, we need to determine the transient A and B peak positions from Fig. 5. Given the relatively low energy resolution of our measurement, we do not have sufficient data points to fit a dispersive function to the B peak region. Instead, we make use of the ground state spectra collected at APS to reduce the dimensionality of the fit in order to reconstruct a difference spectra and extract the peak positions.

The reconstructed difference spectrum uses the peak and edge characteristics of the ground state FeRu spectrum and model complexes along with fitted peak and edge positions of the excited state spectrum. All of the relevant fit parameters are given in Tables S18 of the Supplementary Information. A detailed discussion of the reconstructed difference spectrum is given in Section 3.7 of the Supplementary Information. The final excited state A, B, and C peak positions are 7113.2 eV, 7115.8 eV, and 7119.5 eV with the reconstrution shown in the lower right panel of Fig. 5. Applying the linear relationship found between the calculated hole charges and peak splittings, we determine that the hole charge on the Fe atom over the time duration of our transient measurement is 0.75 ± 0.18.

Similar calculations of the Fe hole charge using the measured and calculated C peak are shown in section 3.10 in the Supplementary Information. We find that the calculated ground state B, C peak splitting does not accurately predict the measurement and therefore we do not rely on this measurement to determine the Fe hole charge. This is largely due to the significant solvent contributions in these transitions, which is also seen in the aquated model complexes.[47,48] However, given the large signal size of the C peak which could improve the signal to noise, future measurements and calculations may find the C peak a useful measure of the electronic structure, which is why we include this analysis.

Our measurement of the Fe hole charge demonstrates how time-resolved HERFD-XANES measurements combined with novel excited-state calculations can provide detailed information about the electron density in excited state mixed-valence metal complexes. We expect

that as energy and time resolution at FEL facilities improves, time-resolved HERFD-XANES measurements will be useful tools for probing electron delocalization. In this case, we can confirm that the MMCT pictured in Fig. S3 of the Supplementary Information is indeed relatively localized and results in a 0.75 ± 0.18 hole charge on the Fe atom.

3   Conclusions

We have performed both time-resolved HERFD-XANES and XES measurements on aqueous FeRu after excitation to a MMCT. We extracted the key dynamics of both the MMCT and BET processes in our system, as summarized in Fig. 8. Following the MMCT, we measured the BET and the vibrational cooling timescales using time-resolved XES. Oscillations in the XES signal also revealed low frequency modes that are an indicator of a ultrafast population transfer back to the ground state during the BET resulting in a vibrationally hot ground state that likely involves Fe-Ru breathing motion. By combining the HERFD-XANES spectrum with state-of-the-art TDDFT calculations of the solvated complex we measured the transient hole charge on the Fe atom to directly measure its mixed valency in order to confirm a relatively localized electron hole density on the Fe atom. These observations show that FeRu has a fast and localized BET that excites a vibrationally hot ground state involving nuclear motion along the bridge. Combining these observations with the ultrafast X-ray scattering measurements of the solvent dynamics in Ref. 40 provides a global view of coupled electronic, vibrational, and solvent motions in a mixed valence complex.

With further FEL enhancements, we expect that the time-resolved HERFD-XANES and XES measurements demonstrated here will become important tools for studying electron delocalization and vibrational excitations in non-equilibrium conditions. This will provide key insights into electron transfer mechanisms and accompanying dynamics in complex molecular systems in realistic environments.
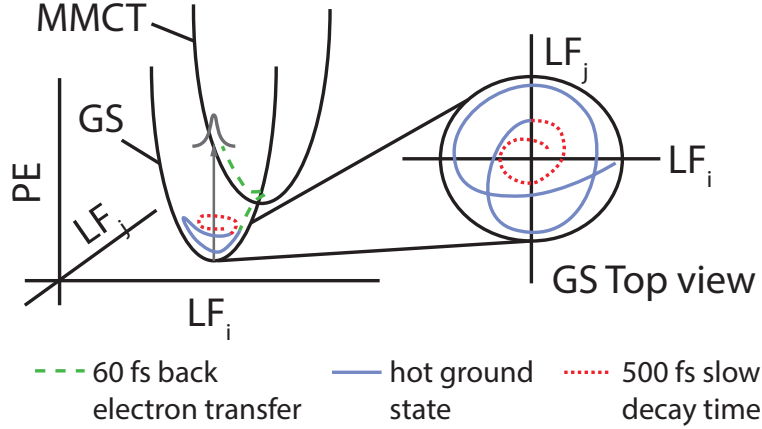
Figure 8: **BET on a potential energy surface.** We have shown evidence that as FeRu returns to the ground state, it settles onto a hot ground state where at least two low frequency modes are excited. These vibrational excitations relax on a 500 fs timescale.

4   Methods

4.1   Optical Pump-X-ray Probe

We performed an optical pump, X-ray probe experiment at the XPP endstation at LCLS.[49] We measured three signals, spectrally resolved emission, total fluorescence yield (TFY), and elastic scattering. In this paper, we focus on the emission signal.

As shown in part (a) of Fig. 1, 30 mM of aqueous FeRu is introduced into the experiment via a 50 μm round jet. A 4 μJ, 40 fs FWHM, 800 nm laser pulse with a 100 by 120 μm focus excites FeRu to the MMCT state. This pulse intensity is within the linear excitation regime, as shown in Fig. S6 of the Supplementary Information. The ensuing dynamics are probed with 45 fs FWHM X-ray pulses at and above the 7.1 keV Fe K-edge at 120 Hz. The time delay between the two pulses is varied from -0.4 ps to 1.5 ps for time scans and the jitter is measured using the XPP timing tool.[49,50] The emission spectra is spectrally resolved with a Rowland spectrometer and image area detector with 0.4 eV resolution.

We performed both time dependent XES and time-resolved HERFD-XANES measurements. Time dependent XES kinetic traces were performed by tuning the incoming X-rays above the Fe K-edge to 8 keV without the monochromator in the so-called "pink-beam" mode

which increases the X-ray flux to 10^{12} photons per pulse. The Rowland spectrometer was tuned to specific emission energies in the $K\alpha_1$ emission line, as shown in Fig. 1, while scanning the pump-probe delay. The emission spectra are then normalized to the total emission measured on the TFY diode. The exact equation defining the XES is given in Eq. 2 of the Supplementary Information.

Time resolved HERFD-XANES measurements were taken by tuning the Rowland spectrometer to the peak of the ground state $K\alpha_1$ emission line while scanning the incident X-ray energy below the Fe K-edge using a 1 eV bandwidth Si(111) channel-cut monochromator, which reduces the X-ray flux by a factor of $\sim$100. The spectrometer intensity is then normalized to the pulse intensity. The equation defining the HERFD-XANES spectra is given in Eq. 5 of the Supplementary Information. During these scans, the nominal pump probe delay was set to 0 fs while the timing jitter between the optical pump and X-ray probe allowed us to effectively scan the time delay. The uncertainty associated with each data point in both the XES and HERFD-XANES measurements is determined by bootstrapping the data set, details of which are given in Section 3.4 of the Supplementary Information.

The X-ray pulses used in this experiment were generated using self-amplified spontaneous emission (SASE). They therefore lack temporal-coherence between X-ray pulses and vary strongly in their characteristics from pulse to pulse. In addition, the position of the jet can move as a function of experimental time. While variation in the X-ray pulses is minimized after the monochromator, we further reduce variation between X-ray shots by removing measurements that strongly vary from the median pulse and jet characteristics using a series of filters that monitor the X-ray pulses and the jet position. These filters include measurements of the TFY, the elastic scattering signal, the pulse intensity, and additional beam diagnostics. Details of the filters applied to both the XES and HERFD-XANES measurements are listed in Tables S5 and S13 respectively of the Supplementary Information.

Both the XES and HERFD-XANES spectra depend on the electronic configuration of the molecule as shown in part (b) of Fig. 1. The red dashed curve represents the initial MMCT

excitation and subsequent BET. The Kα_1 XES spectra measures the $2p_{3/2}$ to 1s fluorescence after the incoming, above edge X-ray photon ejects a 1s electron. The XES spectra will therefore measure the $2p_{3/2}$ to 1s energy splitting, as we will show, is sensitive to the t_{2g} occupancy and the geometric configuration of the molecule. During the HERFD-XANES measurement, the peak Kα_1 emission intensity is largely determined by the absorption of the incoming pre-edge X-ray photon. Critically, the A peak monitors the vacancy state of the t2g level and its position will vary during the MMCT and BET as the oxidation state of the Fe atom changes. We will show that this property allows us to measure the electronic density about the Fe atom and therefore the mixed valency of the FeRu molecule.

4.2   Static X-ray Absorption of Aquated Model Complexes

We use two model complexes in water, ferrocyanide ($[Fe^{II}(CN)_6]^{4-}$) and ferricyanide ($[Fe^{III}(CN)_6]^{3-}$), to study how the oxidation state of Fe ligand complexes affects the Fe K-edge XES and HERFD-XANES spectra. Static X-ray absorption and emission measurements of the model complexes were measured at beamline 7-ID-D at the Advanced Photon Source (APS) at Argonne National Laboratory using the same conditions and as described in Ref. 47. Briefly, 400 mM solutions of $K_4Fe^{II}(CN)_6$ and $K_3Fe^{III}(CN)_6$ were introduced to the X-ray beam via a 200 μm liquid jet. X-ray fluorescence was dispersed with a Ge440 crystal analyzer in a von Hamos geometry and then detected with a silicon diode array detector. The emission spectra were measured while the incident photon energy was scanned below the Fe K-edge.

4.3   Calculations

All ground and excited state calculations, were performed with the NWChem computational chemistry program.[51,52] These simulations were performed at the density functional theory (DFT) and time-dependent density functional theory (TDDFT) levels of theory. Our choice of DFT and TDDFT, which offer a good balance between accuracy and computa-

tional performance cost, was motivated by the sizes of the large explicitly solvated transition metal clusters considered in this study. We have successfully used the same approach in other studies, where we have shown the importance of explicit solvation, leading up to this work.[46,53] Comparisons between experimental and calculated ground state IR, UV-Vis, and Fe K-edge XANES of FeRu are shown in the Supplementary Information in Figs. S1, S2, and S4, respectively.

4.3.1 Quantum-Mechanics/Molecular Mechanics (QM/MM) Simulations

A QM/MM simulation of FeRu was first performed in the ground state.[53] The complex was solvated in a cubic water box of size 53 Å consisting of 4992 water molecules with a density of ~1 g/cm^3. A single potassium cation (K$^+$) was placed in the water solvent to charge balance the 1- charged FeRu complex. The FeRu complex was designated the quantum mechanics (QM) region, and the water molecules with the K$^+$ cation was designated the molecular mechanics (MM) region in subsequent QM/MM simulations. The classical force-field used for the water molecules was the extended single point charge water model (SPC/E) of Berendsen and co-workers.[54] The single K$^+$ cation was represented with the SPC/E-compatible K$^+$ force field of Joung and Cheatham.[55] For the QM region, van der Waals parameters for the C, N, and H atoms were obtained from the general AMBER force-field (GAFF) set.[56] The Fe and Ru atoms in the complex do not interact directly with the water solvent and are therefore assigned the Fe^{2+} (feo) van der Waals parameters of the CLAYFF forcefield of Cygan and co-workers to approximate the relatively short Fe/Ru-ligand van der Waals interactions.[57] Lorentz-Berthelot mixing and AMBER 1-4 rules for non-bonding interactions apply. Following the preparation of the solvated system and assignment of force-field parameters, the entire system was optimized.

The QM region was treated with DFT with the global hybrid PBE0 exchange-correlation density functional.[58,59] The 6-311G** basis set was used for the light atoms, H, C, and N,[60] and the Stuttgart scalar relativistic basis set and effective core potentials (ECP) were used

for the Fe and Ru atoms.[61,62] The SHAKE algorithm[63] was applied to the water molecules to constrain the bond lengths and bond angle, as prescribed by the SPC/E potential. The Coulombic interaction was set to 1.2 nm. The QM/MM interaction zone surrounding the complex was set to 2.0 nm. Geometry optimization was performed cyclically with a maximum of 10 QM region Broyden-Fletcher-Goldfarb-Shanno (BFGS) iterations followed by a maximum of 3000 MM region steepest-descent (SD) iterations. This cycle was repeated for a maximum of 5 times until convergence. Following optimization, QM/MM molecular dynamics were performed. Initially, the complex was held fixed and the water solvent was allowed to equilibrate over 10 ps with a time step of 2 fs and using the Berendsen thermostat[64] for NVT simulations at 298.15 K. After this initial equilibration, the complex was allowed to equilibrate with the solvent for 1 ps and a time step of 0.25 fs. Following 1 ps, QM/MM dynamics of the entire system was run for another 20 ps. These ground state calculations were performed with the NWChem QM/MM module.

4.3.2 TDDFT Calculations

For the TDDFT calculations of the FeRu complex, clusters were extracted from the equilibrated QM/MM trajectory. Clusters ($\approx$ 238 atoms) were constructed by centering the transition metal complex center as well as a 4Å thick shell of explicit water molecules surrounding the complex. These clusters are sufficiently large to capture the ground state properties compared with experiment as seen in Figs. S1, S2, and S4 of the Supplementary Information. Excited state geometries were computed by optimizing these clusters on the MMCT surface and Fe K-edge XANES calculations were performed on these excited-state geometries to obtain transient spectra. The MMCT excited state optimizations were performed with TDDFT gradients,[65] while the XANES calculations were performed with the restricted excitation window TDDFT approach,[66] including higher-order contributions to the oscillator strengths to capture the quadrupolar nature of the pre-edge transitions at the Fe K-edge. To follow the electron transfer, Mulliken and Löwdin populations were calculated

on the Fe and Ru atoms to track the hole charges as the system evolved along the MMCT surface.

For consistency, the PBE0 exchange-correlation density functional was also used in all the TDDFT calculations,[58,59] along with the 6-311G** basis set for the light atoms, H, C, and N,[60] and the Stuttgart scalar relativistic basis set and effective core potentials (ECP) for Fe and Ru,[61,62] respectively. The Fe K-edge XANES calculations were performed with the Fe atom represented with the all-electron Sapporo-TZP-2012 basis set.[67] Details of how the calculated XANES spectra are compared to the HERFD-XANES spectra are discussed in Section 2.3.

5   Author Contributions

C.L.-S. performed the experimental analysis. Z.W.F., K.S.K., R.A.-M., J.C., M.C., J.D.G., J.M.G., K.H., T.K., J.H.L., M.R., D.S., A. C.-H., R.S., and M.K. participated in the design and implementation of the LCLS experiment. G.D., A.M.M., S.H.S., Z.W.F., and M.K. participated in the design and implementation of the APS experiment. N.G. and A.A. performed the QM/MM DFT and TDDFT calculations. All authors participated in the interpretation and discussion of the results. C.L.-S., N.G., and M.K. wrote the article.

References

(1) Heinz, T. et al. *Basic Energy Sciences Roundtable: Opportunities for Basic Research at the Frontiers of XFEL Ultrafast Science*; 2017; p 1616251.

(2) Fleming, G. R.; Ratner, M. A. *Physics Today* **2008**, *61*, 28–33.

(3) Reid, P. J.; Silva, C.; Barbara, P. F.; Karki, L.; Hupp, J. T. *The Journal of Physical Chemistry* **1995**, *99*, 2609–2616.

(4) Wang, C.; Mohney, B. K.; Akhremitchev, B. B.; Walker, G. C. *The Journal of Physical Chemistry A* **2000**, *104*, 4314–4320, Publisher: American Chemical Society.

(5) Courtney, T. L.; Fox, Z. W.; Estergreen, L.; Khalil, M. *The Journal of Physical Chemistry Letters* **2015**, *6*, 1286–1292.

(6) Lynch, M. S.; Van Kuiken, B. E.; Daifuku, S. L.; Khalil, M. *The Journal of Physical Chemistry Letters* **2011**, *2*, 2252–2257.

(7) Lynch, M. S.; Slenkamp, K. M.; Khalil, M. *The Journal of Chemical Physics* **2012**, *136*, 241101, Publisher: American Institute of Physics.

(8) Slenkamp, K. M.; Lynch, M. S.; Van Kuiken, B. E.; Brookes, J. F.; Bannan, C. C.; Daifuku, S. L.; Khalil, M. *The Journal of Chemical Physics* **2014**, *140*, 084505, Publisher: American Institute of Physics.

(9) Fox, Z. W.; Blair, T. J.; Khalil, M. *The Journal of Physical Chemistry Letters* **2020**, *11*, 1558–1563, Publisher: American Chemical Society.

(10) Tominaga, K.; Kliner, D. A. V.; Johnson, A. E.; Levinger, N. E.; Barbara, P. F. *The Journal of Chemical Physics* **1993**, *98*, 1228–1243, Publisher: American Institute of Physics.

(11) Demadis, K. D.; Hartshorn, C. M.; Meyer, T. J. *Chemical Reviews* **2001**, *101*, 2655–2686.

(12) Kubiak, C. P. *Inorganic Chemistry* **2013**, *52*, 5663–5676.

(13) Kaupp, M.; Renz, M.; Parthey, M.; Stolte, M.; Würthner, F.; Lambert, C. *Physical Chemistry Chemical Physics* **2011**, *13*, 16973.

(14) Watzky, M. A.; Endicott, J. F.; Song, X.; Lei, Y.; Macatangay, A. *Inorganic Chemistry* **1996**, *35*, 3463–3473.

(15) Robin, M. B.; Day, P. In *Advances in Inorganic Chemistry and Radiochemistry*; Emeléus, H. J., Sharpe, A. G., Eds.; Academic Press, 1968; Vol. 10; pp 247–422.

(16) Bressler, C.; Chergui, M. *Chemical Reviews* **2004**, *104*, 1781–1812.

(17) Bauer, M. *Physical Chemistry Chemical Physics* **2014**, *16*, 13827–13837, Publisher: Royal Society of Chemistry.

(18) A. Lima, F.; Bjornsson, R.; Weyhermüller, T.; Chandrasekaran, P.; Glatzel, P.; Neese, F.; DeBeer, S. *Physical Chemistry Chemical Physics* **2013**, *15*, 20911–20920, Publisher: Royal Society of Chemistry.

(19) Hämäläinen, K.; Siddons, D. P.; Hastings, J. B.; Berman, L. E. *Physical Review Letters* **1991**, *67*, 2850–2853, Publisher: American Physical Society.

(20) Tanaka, S.; Okada, K.; Kotani, A. *Journal of the Physical Society of Japan* **1994**, *63*, 2780–2787, Publisher: The Physical Society of Japan.

(21) Heijboer, W. M.; Glatzel, P.; Sawant, K. R.; Lobo, R. F.; Bergmann, U.; Barrea, R. A.; Koningsberger, D. C.; Weckhuysen, B. M.; de Groot, F. M. F. *The Journal of Physical Chemistry B* **2004**, *108*, 10002–10011, Publisher: American Chemical Society.

(22) Guo, M.; Prakash, O.; Fan, H.; Groot, L. H. M. d.; Freyr Hlynsson, V.; Kaufhold, S.; Gordivska, O.; Velásquez, N.; Chabera, P.; Glatzel, P.; Wärnmark, K.; Persson, P.; Uhlig, J. *Physical Chemistry Chemical Physics* **2020**, *22*, 9067–9073, Publisher: Royal Society of Chemistry.

(23) Muller, P.; Neuba, A.; Flörke, U.; Henkel, G.; Kühne, T. D.; Bauer, M. *The Journal of Physical Chemistry A* **2019**, *123*, 3575–3581, Publisher: American Chemical Society.

(24) Seddon, E. A.; Clarke, J. A.; Dunning, D. J.; Masciovecchio, C.; Milne, C. J.; Parmigiani, F.; Rugg, D.; Spence, J. C. H.; Thompson, N. R.; Ueda, K.; Vinko, S. M.; Wark, J. S.; Wurth, W. *Reports on Progress in Physics* **2017**, *80*, 115901, Publisher: IOP Publishing.

(25) Huang, Z.; Kim, K.-J. *Physical Review Special Topics - Accelerators and Beams* **2007**, *10*, 034801, Publisher: American Physical Society.

(26) Haldrup, K. et al. *The Journal of Physical Chemistry B* **2016**, *120*, 1158–1168, Publisher: American Chemical Society.

(27) Kunnus, K. et al. *Structural Dynamics* **2016**, *3*, 043204, Publisher: American Institute of Physics.

(28) Wernet, P. et al. *Nature* **2015**, *520*, 78–81, Number: 7545 Publisher: Nature Publishing Group.

(29) Zhang, W. et al. *Nature* **2014**, *509*, 345–348, Number: 7500 Publisher: Nature Publishing Group.

(30) Ogi, Y. et al. *Structural Dynamics* **2015**, *2*, 034901, Publisher: American Institute of Physics.

(31) Vankó, G. et al. *The Journal of Physical Chemistry C* **2015**, *119*, 5888–5902, Publisher: American Chemical Society.

(32) Canton, S. E. et al. *Nature Communications* **2015**, *6*, 6359, Number: 1 Publisher: Nature Publishing Group.

(33) Kunnus, K. et al. *Nature Communications* **2020**, *11*, 634.

(34) Lemke, H. T. et al. *The Journal of Physical Chemistry A* **2013**, *117*, 735–740.

(35) Shelby, M. L.; Lestrange, P. J.; Jackson, N. E.; Haldrup, K.; Mara, M. W.; Stickrath, A. B.; Zhu, D.; Lemke, H. T.; Chollet, M.; Hoffman, B. M.; Li, X.; Chen, L. X. *Journal of the American Chemical Society* **2016**, *138*, 8752–8764, Publisher: American Chemical Society.

(36) Miller, N. A.; Deb, A.; Alonso-Mori, R.; Garabato, B. D.; Glownia, J. M.; Kiefer, L. M.; Koralek, J.; Sikorski, M.; Spears, K. G.; Wiley, T. E.; Zhu, D.; Kozlowski, P. M.; Kubarych, K. J.; Penner-Hahn, J. E.; Sension, R. J. *Journal of the American Chemical Society* **2017**, *139*, 1894–1899, Publisher: American Chemical Society.

(37) Kambhampati, P.; Son, D. H.; Kee, T. W.; Barbara, P. F. *The Journal of Physical Chemistry A* **2000**, *104*, 10637–10644.

(38) Tivanski, A. V.; Wang, C.; Walker, G. C. *The Journal of Physical Chemistry A* **2003**, *107*, 9051–9058.

(39) Watson, D. F.; Tan, H. S.; Schreiber, E.; Mordas, C. J.; Bocarsly, A. B. *The Journal of Physical Chemistry A* **2004**, *108*, 3261–3267.

(40) Biasin, E. et al. *Accepted for publication in Nature Chemistry*

(41) Glatzel, P.; Bergmann, U. *Coordination Chemistry Reviews* **2005**, *249*, 65–95.

(42) Vacher, M.; Kunnus, K.; Delcey, M. G.; Gaffney, K. J.; Lundberg, M. *Structural Dynamics* **2020**, *7*, 044102, Publisher: American Institute of Physics.

(43) Ruhman, S.; Joly, A.; Nelson, K. *IEEE Journal of Quantum Electronics* **1988**, *24*, 460–469.

(44) Ruhman, S.; Joly, A. G.; Nelson, K. A. *The Journal of Chemical Physics* **1987**, *86*, 6563–6565.

(45) Lima, F. A.; Bjornsson, R.; Weyhermüller, T.; Chandrasekaran, P.; Glatzel, P.; Neese, F.; DeBeer, S. *Physical Chemistry Chemical Physics* **2013**, *15*, 20911–20920.

(46) Van Kuiken, B. E.; Valiev, M.; Daifuku, S. L.; Bannan, C.; Strader, M. L.; Cho, H.; Huse, N.; Schoenlein, R. W.; Govind, N.; Khalil, M. *The Journal of Physical Chemistry A* **2013**, *117*, 4444–4454.

(47) Ross, M.; Andersen, A.; Fox, Z. W.; Zhang, Y.; Hong, K.; Lee, J.-H.; Cordones, A.; March, A. M.; Doumy, G.; Southworth, S. H.; Marcus, M. A.; Schoenlein, R. W.; Mukamel, S.; Govind, N.; Khalil, M. *The Journal of Physical Chemistry B* **2018**, *122*, 5075–5086.

(48) Penfold, T. J.; Reinhard, M.; Rittmann-Frank, M. H.; Tavernelli, I.; Rothlisberger, U.; Milne, C. J.; Glatzel, P.; Chergui, M. *The Journal of Physical Chemistry A* **2014**, *118*, 9411–9418.

(49) Glownia, J. M.; Gumerlock, K.; Lemke, H. T.; Sato, T.; Zhu, D.; Chollet, M. *Journal of Synchrotron Radiation* **2019**, *26*, 685–691, Number: 3 Publisher: International Union of Crystallography.

(50) Chollet, M. et al. *Journal of Synchrotron Radiation* **2015**, *22*, 503–507.

(51) Valiev, M.; Bylaska, E.; Govind, N.; Kowalski, K.; Straatsma, T.; Dam, H. V.; Wang, D.; Nieplocha, J.; Aprà, E.; Windus, T.; de Jong, W. *Comput. Phys. Commun.* **2010**, *181*, 1477 – 1489.

(52) Aprà, E. et al. *The Journal of Chemical Physics* **2020**, *152*, 184102.

(53) Ross, M.; Andersen, A.; Fox, Z. W.; Zhang, Y.; Hong, K.; Lee, J.-H.; Cordones, A.; March, A. M.; Doumy, G.; Southworth, S. H.; Marcus, M. A.; Schoenlein, R. W.; Mukamel, S.; Govind, N.; Khalil, M. *The Journal of Physical Chemistry B* **2018**, *122*, 5075–5086.

(54) Berendsen, H. J. C.; Grigera, J. R.; Straatsma, T. P. *The Journal of Physical Chemistry* **1987**, *91*, 6269–6271.

(55) Joung, I. S.; Cheatham, T. E. *The Journal of Physical Chemistry B* **2008**, *112*, 9020–9041.

(56) Wang, J.; Wolf, R. M.; Caldwell, J. W.; Kollman, P. A.; Case, D. A. *Journal of Computational Chemistry* **2004**, *25*, 1157–1174.

(57) Cygan, R. T.; Liang, J.-J.; Kalinichev, A. G. *The Journal of Physical Chemistry B* **2004**, *108*, 1255–1266.

(58) Perdew, J. P.; Ernzerhof, M.; Burke, K. *The Journal of Chemical Physics* **1996**, *105*, 9982–9985.

(59) Adamo, C.; Barone, V. *The Journal of Chemical Physics* **1999**, *110*, 6158–6170.

(60) Krishnan, R.; Binkley, J. S.; Seeger, R.; Pople, J. A. *The Journal of Chemical Physics* **1980**, *72*, 650–654.

(61) Dolg, M.; Wedig, U.; Stoll, H.; Preuss, H. *The Journal of Chemical Physics* **1987**, *86*, 866–872.

(62) Andrae, D.; Häußermann, U.; Dolg, M.; Stoll, H.; Preuß, H. *Theoretica chimica acta* **1990**, *77*, 123–141.

(63) Ryckaert, J.-P.; Ciccotti, G.; Berendsen, H. J. *Journal of Computational Physics* **1977**, *23*, 327 – 341.

(64) Berendsen, H. J. C.; Postma, J. P. M.; van Gunsteren, W. F.; DiNola, A.; Haak, J. R. *The Journal of Chemical Physics* **1984**, *81*, 3684–3690.

(65) Silverstein, D. W.; Govind, N.; Van Dam, H. J.; Jensen, L. *Journal of chemical theory and computation* **2013**, *9*, 5490–5503.

(66) Lopata, K.; Van Kuiken, B. E.; Khalil, M.; Govind, N. *Journal of Chemical Theory and Computation* **2012**, *8*, 3284–3292.

(67) Noro, T.; Sekiya, M.; Koga, T. *Theoretical Chemistry Accounts* **2012**, *131*, 1124.

Supplementary Information: Femtosecond X-ray Spectroscopy Directly Quantifies Transient Excited State Mixed Valency and Subsequent Vibronic Dynamics

Chelsea Liekhus-Schmaltz,[*,†] Zachary W. Fox,[†] Amity Andersen,[‡] Kasper S. Kjaer,[¶,§] Roberto Alonso-Mori,[‖] Elisa Biasin,[¶] Julia Carlstad,[⊥] Matthieu Chollet,[‖] James D. Gaynor,[⊥] James M. Glownia,[‖] Kiryong Hong,[#] Thomas Kroll,[@] Jae Hyuk Lee,[△,▽] Benjamin I. Poulter,[†] Marco Reinhard,[¶] Dimosthenis Sokaras,[@] Yu Zhang,[††,‡‡] Gilles Doumy,[¶¶] Anne Marie March,[¶¶] Stephen H. Southworth,[¶¶] Shaul Mukamel,[††] Amy Cordones-Hahn,[¶] Robert W. Schoenlein,[¶,‖] Niranjan Govind,[*,§§] and Munira Khalil[*,†]

†*Department of Chemistry, University of Washington, Seattle, WA, USA*

‡*Environmental Molecular Sciences Laboratory, Pacific Northwest National Laboratory, Richland, Washington 99352, USA*

¶*Stanford PULSE Institute, SLAC National Accelerator Laboratory, Menlo Park, CA 94025, USA*

§*Technical University of Denmark, Department of Physics, Fysikvej 307, DK-2800 Kongens Lyngby, Denmark*

‖*LCLS, SLAC National Accelerator Laboratory, Menlo Park, CA 94025, USA*

⊥College of Chemistry, University of California, Berkeley, CA 94720, USA

#Gas Metrology Group, Korea Research Institute of Standards and Science, Daejeon 34113, Republic of Korea

@SSRL, SLAC National Accelerator Laboratory, Menlo Park, CA 94025, USA

△Ultrafast X-ray Science Laboratory, Chemical Sciences Division, Lawrence Berkeley National Laboratory, Berkeley, CA 94820, USA

∇Pohang Accelerator Laboratory, Pohang, 37673, Republic of Korea

††Department of Chemistry and Physics & Astronomy, University of California, Irvine, CA 92697, USA

‡‡Q-Chem Inc., 6601 Owens Dr, Pleasanton, CA 94588, USA

¶¶Chemical Sciences and Engineering Division, Argonne National Laboratory, Lemont, IL, 60439, USA

§§Physical and Computational Sciences Directorate, Pacific Northwest National Laboratory, Richland, WA, 99352, USA

E-mail: cliekhus@uw.edu; niri.govind@pnnl.gov; mkhalil@uw.edu

Contents

1 Ground state FeRu IR, UV-Vis, and, K-edge XANES spectra

1.1 Calculated and experimental ground state IR spectra

The steady-state FTIR spectra of 12.5 mM FeRu solution was collected with a JASCO FT/IR 4100 instrument with a 50 micron pathlength. The spectral resolution was $2\,\mathrm{cm}^{-1}$. The water background is subtracted from the spectrum. The comparison between the calculated and experimental IR spectra is shown in Fig. S1.
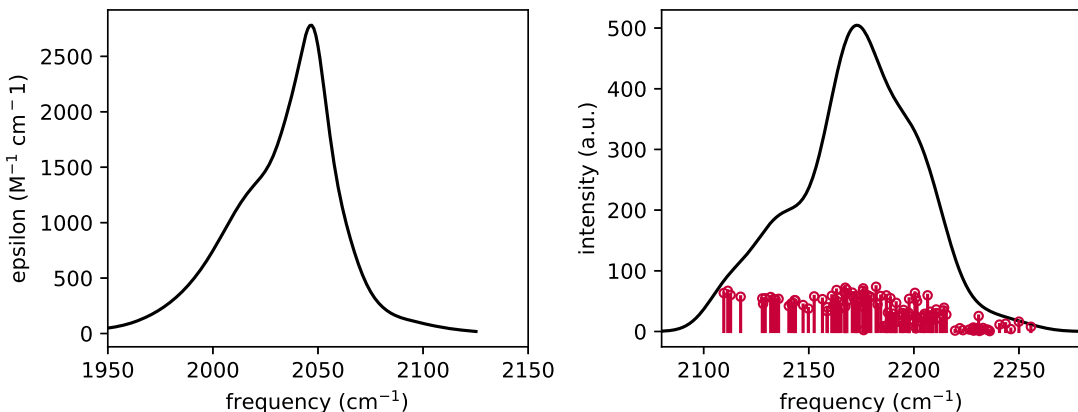
Figure S1: **IR spectra.** Shown in the left panel is the experimental FTIR spectra of FeRu. The right panel shows the unshifted broadened calculated IR spectra. The spectra is broadened by $10\,\mathrm{cm}^{-1}$.

1.2 Calculated and experimental ground state UV-Vis spectra

The steady-state ground state UV-Vis spectra of 12.5 mM FeRu solution was collected with a JASCO V630 spectrometer with a 50 micron pathlength. The spectral resolution was 0.5 nm. The broadened calculated UV-Vis spectra is compared to the experimental UV-Vis spectra in Fig. S2 with the transition density shown in Fig. S3.
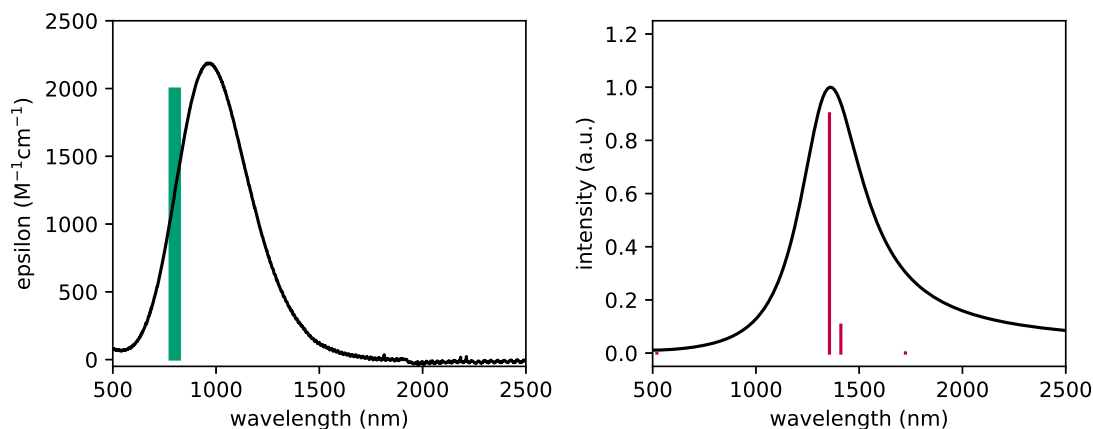
Figure S2: **UV-Vis spectra.** Shown in the left panel is the experimental UV-Vis spectra with the excitation region shown in the green rectangle. The right panel shows the unshifted, broadened calculated UV-Vis spectra. The spectra is broadened by 0.25 eV.
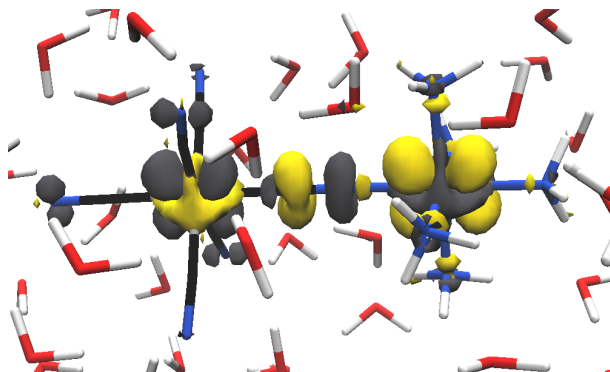

Figure S3: **MMCT transition density.** The electronic transition density associated with the strongest transition line in Fig. S2 is shown; the Fe atom being on the left and the Ru atom being on the right. An accumulation of charge is shown in yellow while a depletion in shown in gray.

1.3 Calculated and experimental ground state Fe K-edge XANES

The ground state XANES spectra of FeRu measured at APS is compared to the calculated XANES spectra here. Details of the APS measurement are shown in Section 4.2 of the main text.
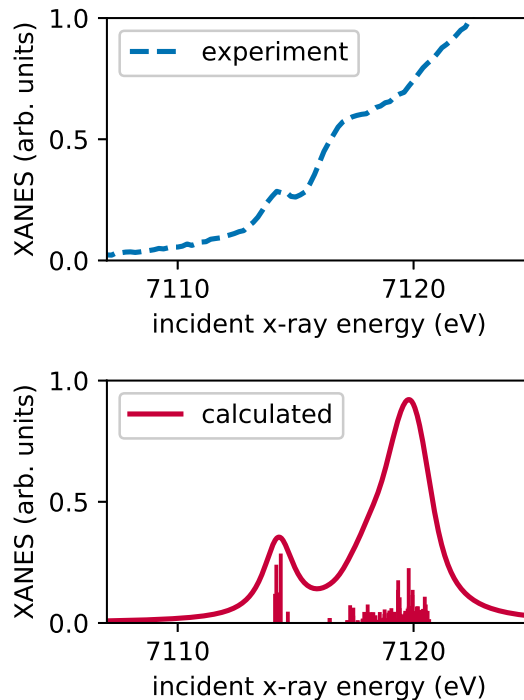
Figure S4: **Fe K-edge XANES.** Shown in the left panel is the experimental Fe K-edge XANES of FeRu. The right panel shows the broadened calculated Fe K-edge XANES. The calculated spectrum has been broadened by 1.5 eV and shifted by 144.7 eV.

1.4 Comparing HERFD-XANES and XANES spectra

To explain in more detail why the HERFD-XANES spectra has a smaller bandwidth, we examine the full resonant inelastic X-ray scattering, RIXS, spectrum of the $([Fe^{III}(CN)_6]^{3-})$ molecule here. The full RIXS spectrum of $([Fe^{III}(CN)_6]^{3-})$ is shown in the upper left corner of Fig. S5, that is the energy resolved emission shown as a function of the incident X-ray energy. The processes involved in this measurement are shown in the lower right panel of Fig. S5, where the incoming X-ray photon core excites the molecule resulting in emission from the 2p orbitals, which is then spectrally resolved. Standard XANES measurements are the projection of the RIXS plane onto the incident X-ray energy axis, as shown in the lower left panel, that is they are normally measured with a TFY or transmission diode. The width of these peaks is largely determined by the lifetime of the 1s hole. The HERFD-XANES measurement is instead a slice along the RIXS plane along the peak of the emission spectra,

6

as shown by the horizontal arrow in the upper left panel of Fig. S5. The resulting spectra, shown in the upper right panel of Fig. S5, has better resolved and narrower peaks, as their bandwidth is largely determined by the 2p lifetime.
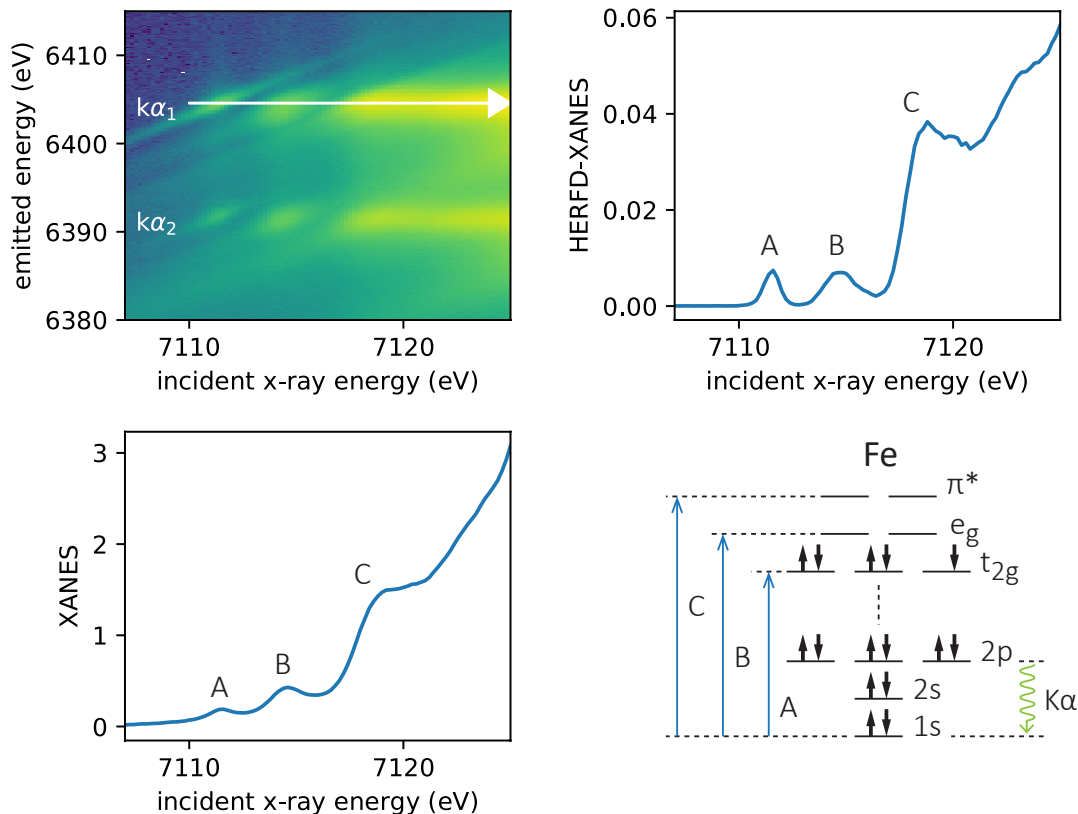

Figure S5: **XANES vs HERFD-XANES comparison.** In the upper left panel is the total RIXS plane of the ($[Fe^{III}(CN)_6]^{3-}$) molecule. A projection along the incident X-ray energy axis provides the standard XANES measurement, shown in the lower left panel. A cut along the emission peak is the HERFD-XANES spectra, shown in the upper right panel. Finally, the processes involved in measuring the RIXS spectra are shown in the lower right panel.

2 X-ray Emission Spectroscopy

2.1 XES filter parameters

As discussed in the main text, X-ray pulses from SASE pulses are necessarily different from shot to shot. As well, the sample jet can move relative to the X-ray focus. It is therefore necessary to filter out dissimilar X-ray shots to form our data set. We apply a series of filters to the XES data to create our final dataset. The number of standard deviations we take from the median for the XES data is shown in Table S5. We apply more stringent constraints on the TFY diode and the Rowland spectrometer intensities since they are essential to this measurement.

Table S5: **Shot to shot filters for XES data.** The filter parameters applied to the XES data are shown here. X-ray shots that are outside the specified number of standard deviations are removed from the analysis.

Value	number of STDs
X-ray intensity	3
Electron bunch energy	1
Integrated CSPAD signal	2
Rowland signal	1
TFY diode signal	1
Time Tool shift value	3
Time Tool signal amplitude	3
Time Tool signal width	3

In addition to filtering on individual parameters, we also apply a linearity filter to the TFY diode and Rowland spectrometer signal. This filter ensures that the TFY diode and Rowland signal are approximately linear to one another. The linearity filter is applied at each timepoint and for the laser off condition separately. We apply a 3 standard deviations of width to our linear filter.

In addition to using the linearity measurement to filter the data, we also use it to remove any offset in the signal due to non-linearities in our detectors at low signal sizes. The full unpumped data set after applying the threshold filters is used to create a linear fit between

the Rowland spectrometer signal and the TFY diode. Ideally, the line should pass through (0,0), however due to non-linearities in the detector response at low signal size, the line is offset. We therefore subtract the offset from our Rowland signal. This step is not necessary for the XANES measurement, since the signal sizes are larger.

2.2 XES definition

The emission spectra, $S_{\text{XES}}(\hbar\nu)$, is computed as the sum of emission intensity collected by the Rowland spectrometer, R_i, at different emission energies, $\hbar\nu$, normalized by the sum of the TFY diode, D_i:

$$S_{\text{XES}}(\hbar\nu) = \frac{\sum_i R_i(\hbar\nu)}{\sum_i D_i} \tag{1}$$

The time-dependent emission signal, $S_{\text{XES}}(\hbar\nu, t)$, at each time, t, is computed as the sum of the emission intensity collected by the Rowland spectrometer at different positions for each X-ray shot, R_i, normalized by the sum of the TFY diode, D_i:

$$S_{\text{XES}}(t) = \frac{\sum_i R_i(\hbar\nu, t)}{\sum_i D_i(t)} \tag{2}$$

The error is determined via bootstrapping, which is discussed in Section 3.4. In contrast to the HERFD-XANES measurement, here we normalize the emission spectral line measurement to the TFY diode. This reduces the noise introduced by the movement of the jet, since both the Rowland signal and the TFY diode signal will be proportionally affected. We are able to do this normalization because the $K\alpha_1$ spectral area is constant over time, and the primary effect we observe are shifts and broadening in the spectra, which can be detected when normalizing by the TFY.

2.3 Determination of Linear Regime

To ensure that we were operating in the linear pump regime, we have monitored the percent change in the emission spectra at 6404 eV as a function of the pump laser energy in Fig. S6. We see that 4 uJ laser energy is within the linear regime. We note that the percent change in emission is smaller than the peak value in Fig. 2 of the main text because we are averaging the XES signal from -30 fs to 30 fs. The noise of this signal, however, is relatively large, and therefore we also rely on linearity measurements given by $K\beta$ and X-ray scattering data detailed in Ref. 1.
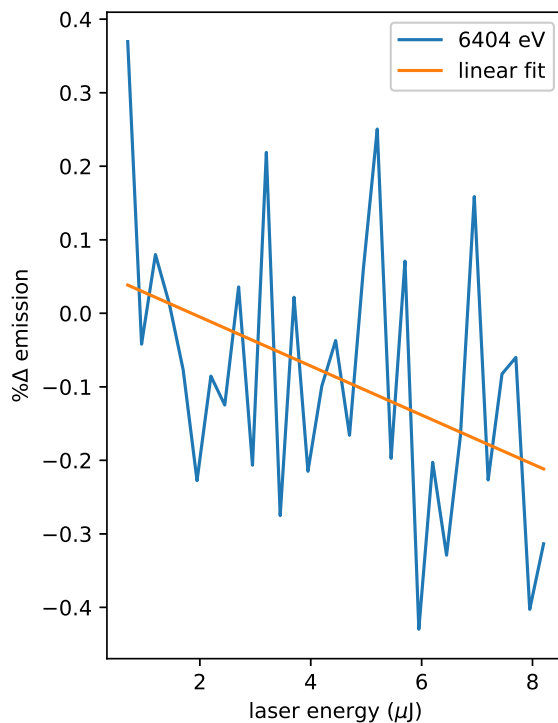
Figure S6: **Pump pulse energy scan.** Percent change in emission intensity as a function of pump pulse energy. A linear fit is shown as an orange line.

2.4 Global fit

Presented below is the equation of fit applied to the time dependent XES signal.

$$F(t) = \left(H(t - t_0) * \left(A_i e^{-(t-t_0)/\tau_1} + B_i e^{-(t-t_0)/\tau_2}\right)\right) \circledast \frac{1}{\sigma\sqrt{2\pi}} e^{-(t-t_0)^2/2\sigma^2}, \tag{3}$$

where $H(t)$ is the Heaviside function, t_0 is the time of overlap, τ_1 is the BET, τ_2 is a second, longer decay time, $2\sqrt{2\ln(2)}\sigma$ is the FWHM IRF, A_i is the amplitude of the τ_1 decay constant for each kinetic trace, i, and B_i is the amplitude of the τ_2 decay constant. The final parameters are given in Table S6.

Table S6: **Global fit parameters.** The fit parameters determined from the global fit in Eq. 3 are shown here.

Parameter	Value
τ_1	58 ± 10 fs
τ_2	510 ± 120 fs
IRF $= 2\sqrt{2\ln(2)}\sigma$	86 ± 7 fs
$A_{6402.7}$	4.4 ± 1 %
$A_{6401.2}$	4.5 ± 1 %
$A_{6404.1}$	-3.8 ± 0.8 %
$B_{6402.7}$	0.12 ± 0.08 %
$B_{6401.2}$	0.06 ± 0.07 %
$B_{6404.1}$	-0.58 ± 0.12

2.5 Static and transient XES spectra

The energy resolved percent difference XES spectra for the MMCT is shown in in the lower panel of Fig. S7 while the ground state XES spectra is shown in the upper panel. The uncertainty of each data point is particularly large. However, the dispersive line shape in this plot is consistent with the time dependent XES plot and the difference plot between the two model complexes in Fig. 2 of the main text.
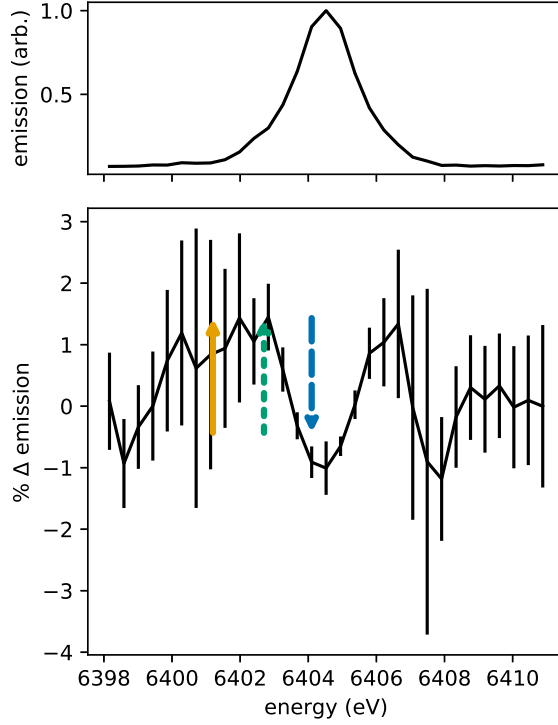
Figure S7: **Excited state $K\alpha_1$ XES spectra.** Shown in the top panel is the ground state XES spectra taken of FeRu at LCLS. The lower panel shows the percent difference XES spectra of the excited state FeRu.

2.6   XES Fourier transforms

In order to motivate a two cosine fit in Fig. 3 of the main text, we apply the Fourier transform to the exponential decay residuals in Fig. 2 of the main text in Fig. S8. Two strong oscillations in the 6404.1 eV signal are apparent, indicating we should use two frequencies in the cosine fit.

2.7   Cosine fit

The residuals of the 6404.1 eV emission kinetic trace are fit to the double cosine function $G(t)$ defined in Eq. 4.

$$G(t) = H(t - t_{on}) * \left(A_1 \cos\left(2\pi\frac{t - t_{on}}{\tau_1}\right) + A_2 \cos\left(2\pi\frac{t - t_{on}}{\tau_2}\right) \right) \circledast e^{-(t-t_0)^2/2\sigma^2} + G_0, \quad (4)$$

12
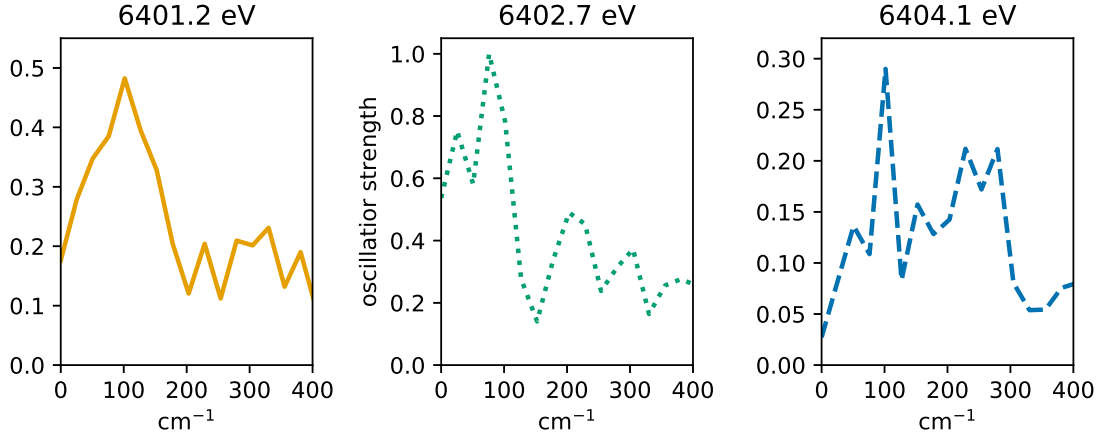
Figure S8: **XES residuals' Fourier transforms.** The Fourier transforms of the XES exponential fit residuals is shown here. We can see evidence for the ∼100 cm^{-1} oscillation in each of the XES lines, as well as a second strong oscillation in the region of 200 to 300 cm^{-1} in the 6404.1 eV emission line.

where $H(t)$ is the Heaviside step function, G_0 is a vertical offset, t_{on} is the time of onset for the oscillations, A_1 and A_2 are oscillation amplitudes, and τ_1 and τ_2 are the periods of oscillation. The resulting fit parameters are shown in Table S8.

Table S8: **Cosine fit parameters.** The fit parameters for the XES kinetic trace residuals are shown here. *The corresponding frequency values for each period is indicated by f.

Parameter	Value
τ_1	300 ± 10 fs
f_1*	109 ± 6 cm^{-1}
τ_2	148 ± 4 fs
f_2*	220 ± 10 cm^{-1}
A_1	-0.06 ± 0.02 %
A_2	-0.1 ± 0.05 %
t_{on}	110 ± 16 fs
G_0	0.009 ± 0.01 %

2.8   Harmonic analysis

In Fig. 3 of the main text we identified a series of low frequency peaks in the time-resolved XES spectra. To associate these peaks with nuclear motion of the solute, we have conducted

a harmonic analysis to identify the ground state low frequency nuclear modes. These low frequency modes are known to be strongly anharmonic, and as a result we are unable to directly relate any particular mode to the observed oscillations, however we expect that one or many of these modes could be involved in the BET process. The modes with the strongest transition amplitude are shown in Fig. S9 and correspond to the red arrows in the calculated low frequency IR transitions shown in Fig. S10. Videos of these harmonics are given online.

2.9   Calculated 1s-2p energy splitting

To confirm that low frequency modes can affect the iron $K\alpha_1$ emission spectra we have calculated the 1s to $2p_{3/2}$ energy splitting of a cooling FeRu molecule on the ground electronic state as a function of time. The result of this calculation after allowing the molecule to equilibriate for 10 ps, is shown in Fig. S11 along with the the Fourier transform from 0 to 500 cm^{-1}. We note that this calculation cannot be directly compared to the oscillations in Fig. 3 of the main text, since the calculation may not be sufficiently vibrationally excited, and the frequencies of the experimental and calculated vibrational modes could therefore be shifted relative to one another. None-the-less we see that the nuclear motion causes a shift of 0.1 eV in the 1s to $2p_{3/2}$ splitting. The Fourier amplitude of the low frequency modes (0 to 250 cm^{-1}) allows us to estimate that the low frequency modes we identify in the main text could shift the 1s to $2p_{3/2}$ energy by 0.03 eV.

While it is computationally expensive to calculate the full XES spectra to recreate the time-resolved XES spectra we measured in Fig. 2 of the main text, we can estimate the effect of this shift on the $K\alpha_1$ spectra at the measured emission energies by manually shifting the measured XES spectra of FeRu and comparing it to the unshifted spectra. Figure S12 shows the percent change in the emission spectra as a function of the emission energy due to a 0.03 eV shift. The percent change at 6404.1 eV is identified and scaled by the excitation fraction to give an estimated overall effect of 0.3% change in our experiment. In comparison, the fitted amplitude of these oscillations was $0.06 \pm 0.02\%$ and $0.1 \pm 0.05\%$.
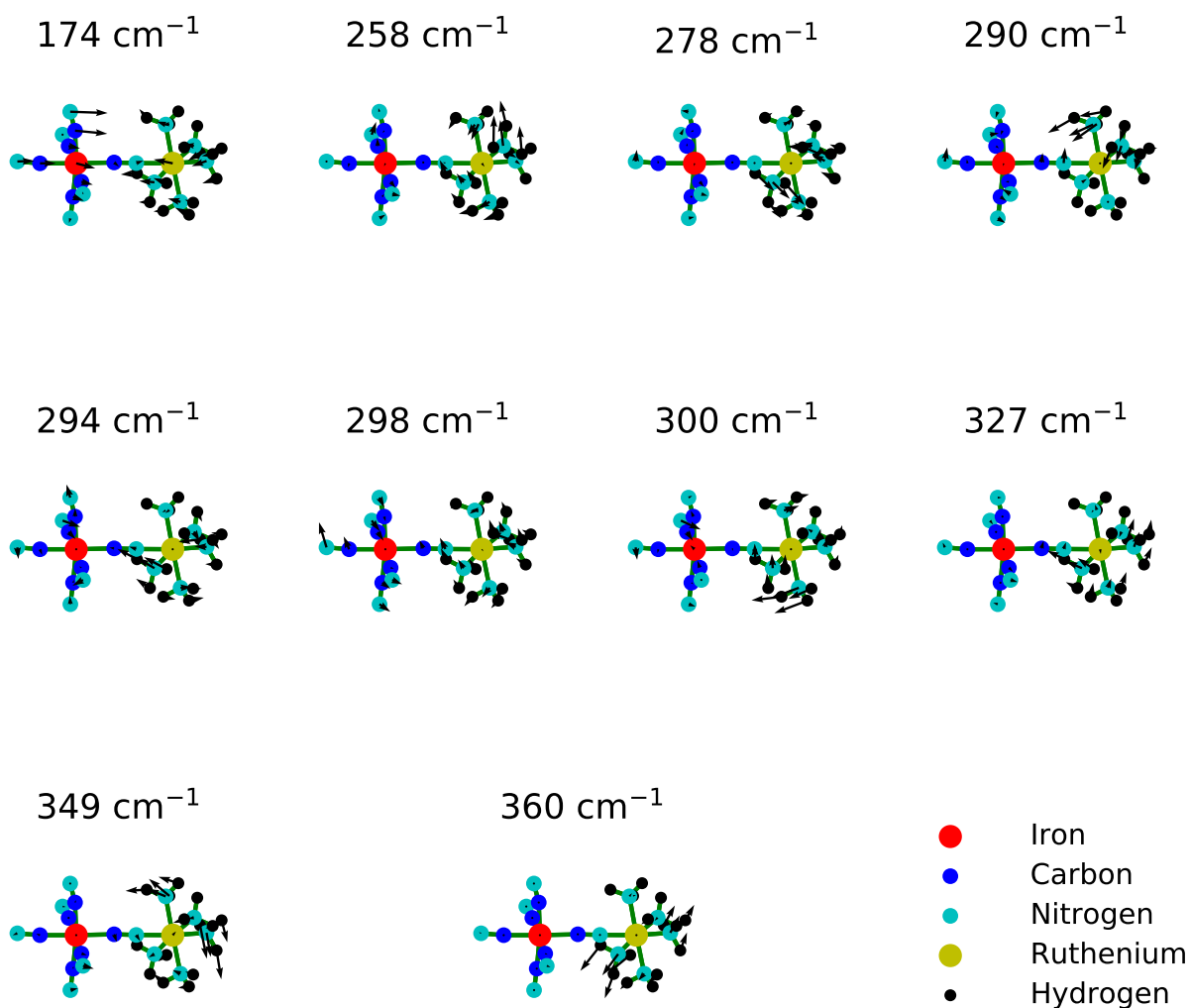
Figure S9: **Harmonic modes' vectors.** The harmonic modes' vectors for the first 10 strongest IR transitions up to 400 cm^{-1} are shown above. The most likely candidate for the slowest oscillation we see in the XES spectra is the 174 cm^{-1} oscillation, which directly involves the Fe atom. Possible oscillations associated with the fast oscillation are the 290, 294, 298, and 300 cm^{-1} which have motion of the cyanide ligands and the bridge.
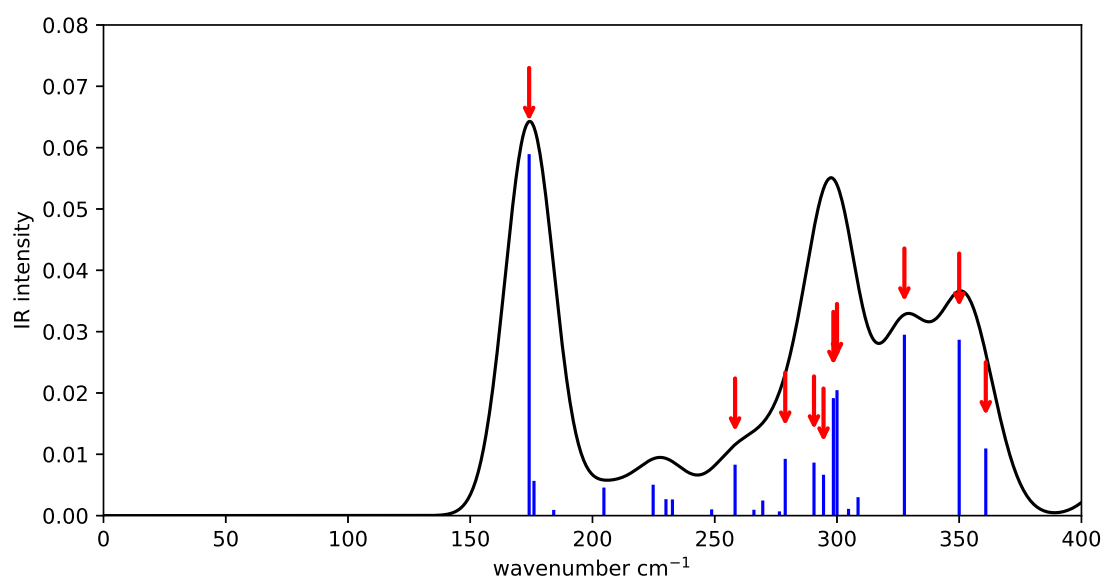
Figure S10: **IR spectra.** The corresponding calculated IR spectra for the oscillations shown in Fig. S9 are shown here. The modes shown in Fig. S9 are indicated by red arrows.
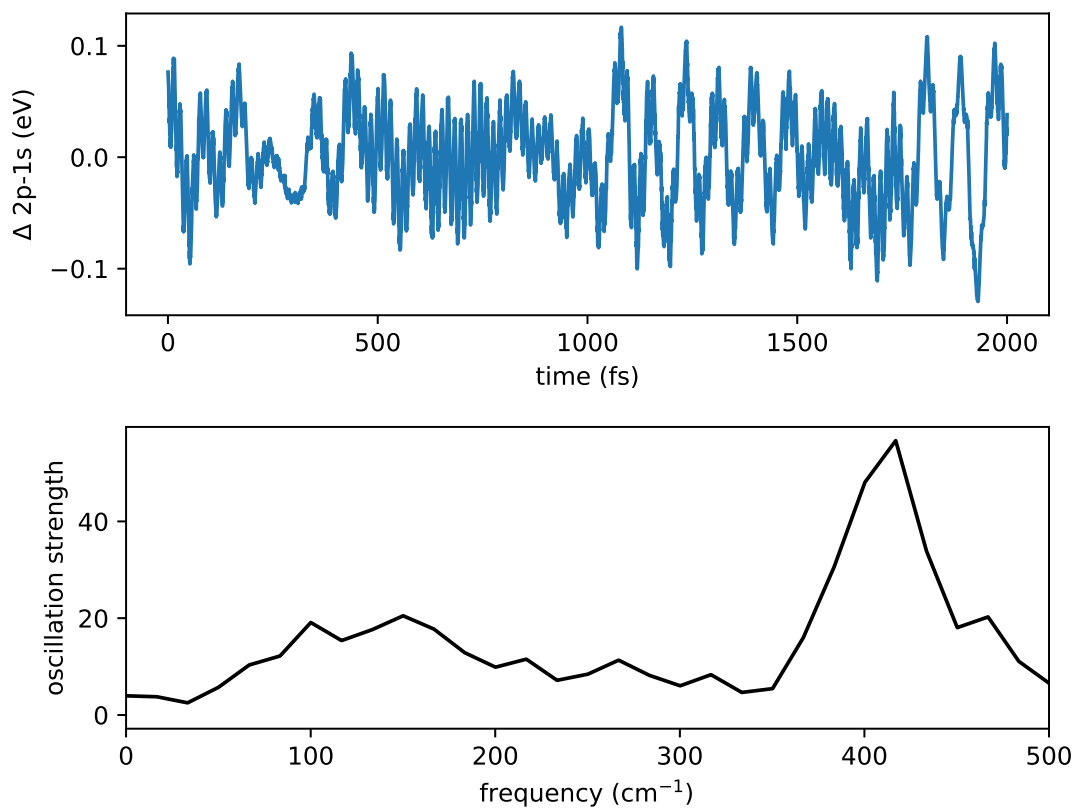
Figure S11: **Calculated time dependent 1s-2p transition.** To evaluate how the Kα_1 spectra will respond to nuclear oscillations, we calculated the 1s-2p energy splitting on a vibrationally cooling FeRu molecule on the ground state. Both the time dependent signal and Fourier transform are shown. We see that oscillations between 100 and 200 cm^{-1} oscillations appear in the calculations. Higher frequency oscillations are also apparent, which we cannot resolve in our experiment.
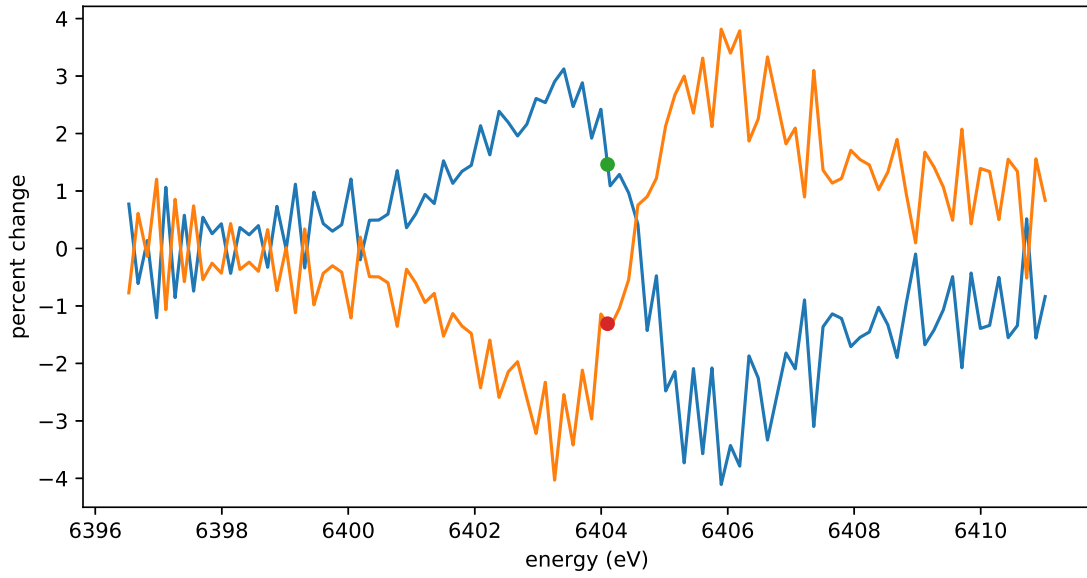
Figure S12: **Kα_1 shift estimate.** To evaluate how a shift in the the Kα_1 spectra will effect the amplitude at 6404.1 eV we find the percent change between the unshifted spectra and the positively shifted spectra (blue) and the negatively shifted spectra (orange). The data points show the percent change at 6404.1 eV.

3 HERFD-XANES

3.1 HERFD-XANES spectra definition

The HERFD-XANES spectra, $S_{\text{XANES}}(\hbar\nu)$, at each incident photon energy, $\hbar\nu$, is computed as the sum the of emission intensities measured by the Rowland spectrometer at the peak of the Kα_1 emission line, R_i, normalized by the sum of all x-ray intensities for each x-ray shot, I_i:

$$S_{\text{XANES}}(\hbar\nu) = \frac{\sum_i R_i(\hbar\nu)}{\sum_i I_i(\hbar\nu)} \tag{5}$$

3.2 Ground state HERFD-XANES spectra

The ground state HERFD-XANES spectra of FeRu, ($[\text{Fe}^{\text{II}}(\text{CN})_6]^{4-}$), and ($[\text{Fe}^{\text{III}}(\text{CN})_6]^{3-}$) measured at APS are shown in Fig. S13 along with the calculated ground state XANES spectra of FeRu. There are two versions of the HERFD-XANES spectra of ($[\text{Fe}^{\text{III}}(\text{CN})_6]^{3-}$). The first version, labeled 'v1' in dotted blue, is given by the emission intensity at the peak of the ($[\text{Fe}^{\text{II}}(\text{CN})_6]^{4-}$) K$\alpha_1$ spectra. The second version, labeled 'v2' in solid blue, is given by the emission intensity at the peak of the ($[\text{Fe}^{\text{III}}(\text{CN})_6]^{3-}$) K$\alpha_1$ spectra, which is the standard method for finding the HERFD-XANES spectra. We compare these two versions because the excited state time resolved HERFD-XANES spectra uses the emission at the ground state Kα_1 maximum. We see that the position of the peaks is not shifted significantly relative to the shifts caused by the change in oxidation state.

3.3 HERFD-XANES filter parameters

X-ray pulses from self-amplified spontaneous emission FEL sources lack temporal coherence between x-ray pulses. In addition, the liquid jet that contains our sample can fluctuate in its position with respect to the X-ray pulses. Therefore, we filter out dissimilar X-ray and jet shots with 8 different shot-to-shot measurements. Each of these values either report on the X-ray pulse characteristic, or the jet character. For each of these measurements, we filter
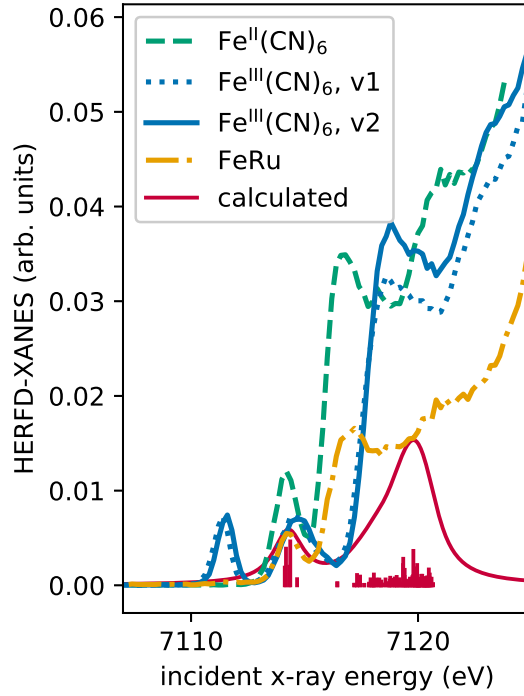
Figure S13: **Ground state HERFD and XANES spectra.** Ground state HERFD-XANES spectra of FeRu, FeII, FeIII taken at APS are show along with the ground state calculated XANES spectra of FeRu. The measurements are normalized by the integral of the full RIXS plane, and the calculation is scaled to match the B peak amplitude.

out measurements that are a certain number of standard deviations away from the median value, as shown in Table S13.

In addition, we filter for a linear response between the x-ray intensity and the TFY signal. This filter is applied separately for each photon energy as well as for the un-pumped shots. The filter on this condition is relatively tight at 0.5 standard deviations from the linear regime.

3.4 Bootstrapping

Bootstrapping allows us to estimate the uncertainty of each data point. A comprehensive guide to bootstrapping can be found in Ref. 2. In brief, bootstrapping is the technique of determining the desired measurement and its uncertainty by finding the mean and standard

Table S13: **Shot to shot filters for HERFD-XANES data.** The filter parameters applied to the HERFD-XANES data are shown here. X-ray shots that are outside the specified number of standard deviations are removed from the analysis.

Value	number of STDs
X-ray intensity	2
Electron bunch energy	1
Integrated CSPAD signal	2
Integrated Rowland signal	2
TFY diode	2
Time Tool shift value	5
Time Tool signal amplitude	2
Time Tool signal width	2

deviation of a collection of recalculated signals from a resampled data set. In more detail, each bootstrapped data set is generated by resampling the raw data with replacement. In our case we have done this 1000 times to generate 1000 different bootstrapped data sets. We have used the same procedure for the XES and HERFD-XANES data, and we use the HERFD-XANES data as an example in this section. The bootstrapped data sets are then used to calculate 1000 different HERFD-XANES spectra, $S^j_{\text{XANES}}(\hbar\nu)$. The final reported value $S_{\text{XANES}}(\hbar\nu)$ is the mean of the bootstrapped data sets, and the uncertainty, $\Delta(\hbar\nu)$ is the standard deviation:

$$S_{\text{XANES}}(\hbar\nu) = \frac{1}{N} \sum_j^N S^j_{\text{XANES}}(\hbar\nu) \tag{6}$$

$$\Delta(\hbar\nu) = \sqrt{\frac{\sum_j^N S^j_{\text{XANES}}(\hbar\nu)}{N}} \tag{7}$$

A figure showing the first 100 bootstrapped datasets can be seen in Fig. S14.

3.5   Comparing XANES and HERFD-XANES spectra

To ensure that the Rowland spectrometer has been properly tuned to the peak of the emission spectra so that we can straightforwardly interpret the HERFD-XANES spectra, we compare the ground state XANES spectra from the TFY diode to the ground state HERFD-XANES
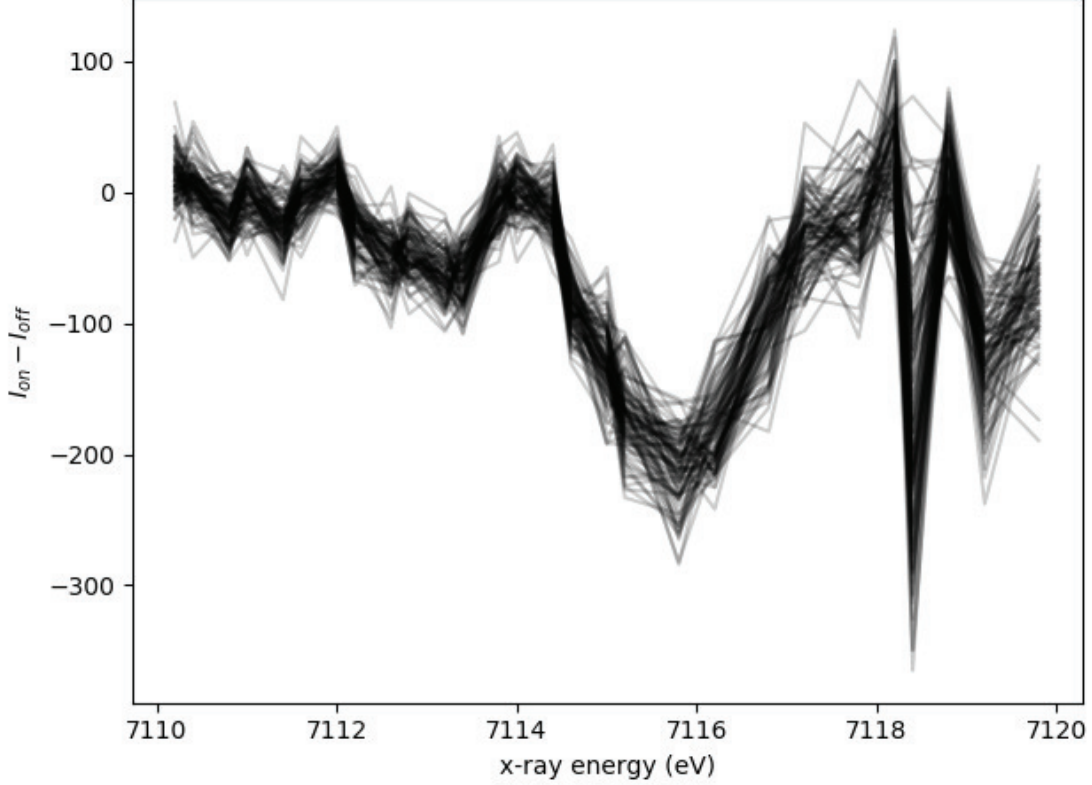
Figure S14: **Bootstrapped dataset subset.** To determine the uncertainty of our measurement, we use the bootstrapping technique to estimate the error. We create 1000 "bootstrapped" datasets by resampling our raw data with replacement 1000 times. We then perform our analysis to each of the datasets and use the mean and standard deviation of each point to report the final value and uncertainty of each data point respectively. Here, the first 100 bootstrap datasets are plotted on top of each other here. We identify the point at 7118.4 eV as having an unusually large amount of error and eliminate it from our dataset. This is because this energy bin contains only $\approx 4\%$ the number of x-ray shots of other energy bins. Each of the other shots have ≈ 1500 shots in them.

spectra. If the Rowland spectrometer is properly aligned, they will each have peaks in the same position. Figure S15 confirms that while there is a difference in shape for both spectra, their peak positions still overlap. Of particular importance is the position of the B peak, which we use directly in our measurement, and is clearly well overlapped between the two measurements.
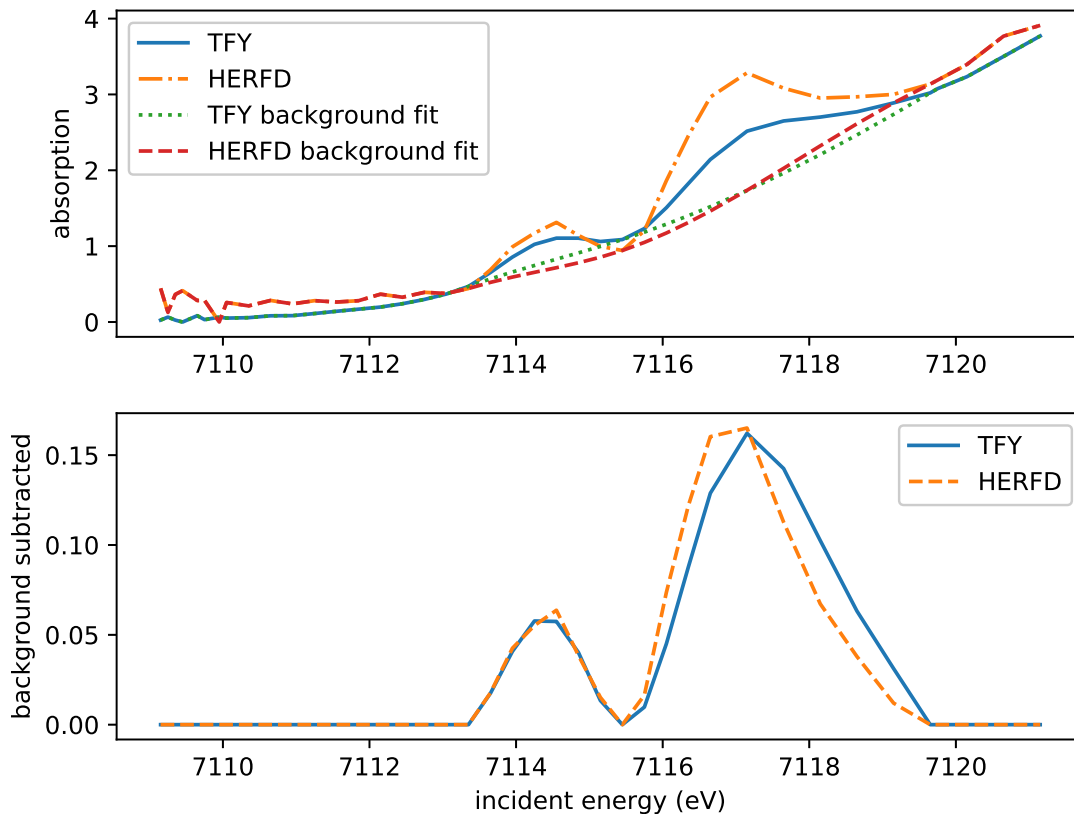

Figure S15: **XANES and HERFD-XANES comparison.** To confirm that we have appropriately set the Rowland spectrometer to the peak of the emission spectra so that we can straightforwardly use the HERFD-XANES measurement, we compare the XANES spectra from the TFY diode to the HERFD-XANES spectra. In the upper panel we see the raw spectra of both signals as well as the background fit we subtract to get the lower panel. The background is spline interpolation of the spectra excluding the peaks. The peak position for both spectra can be compared in the lower panel, where we see that in fact the B and C peaks are in alignment.

3.6 Molecular orbitals plots

Several different molecular orbitals contribute to the A, B, and C peaks, and we display these molecular orbitals here. We see that the A peak involves an orbital that is local to both the Fe and Ru atom, as well as the cyanide bridge. The B peak has contributions from orbitals that are much more delocalized throughout the molecule compared to the A peak. These orbitals have contributions into the solvent as well. The C peak involves molecular orbitals are delocalized from the molecule and involve the solvent.
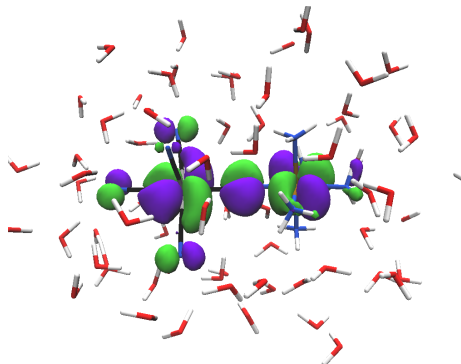
Figure S16: **A peak molecular orbitals.** Molecular orbital associated with the A peak, calculated at an Fe hole charge of 0.68. This orbital has an 86% contribution.

3.7 HERFD-XANES reconstruction details

The main text briefly described the reconstruction technique used to determine the peak positions of the excited state HERFD-XANES FeRu spectra. A more detailed description follows. Both the ground state and excited state in the reconstruction are given by Eq. 5, gaussian peaks overlaid on an error function to represent the Fe K-edge. The position, width, and amplitude of the ground state peaks are given by the APS ground state spectra of FeRu, which had higher signal to noise. The edge characteristics of the ground state FeRu Fe K-edge is given by the LCLS ground state HERFD-XANES spectra, which varies slightly from the APS measurement due to variations in the detector characteristics. The edge characteristics of the excited state are given by the ground state LCLS HERFD-XANES
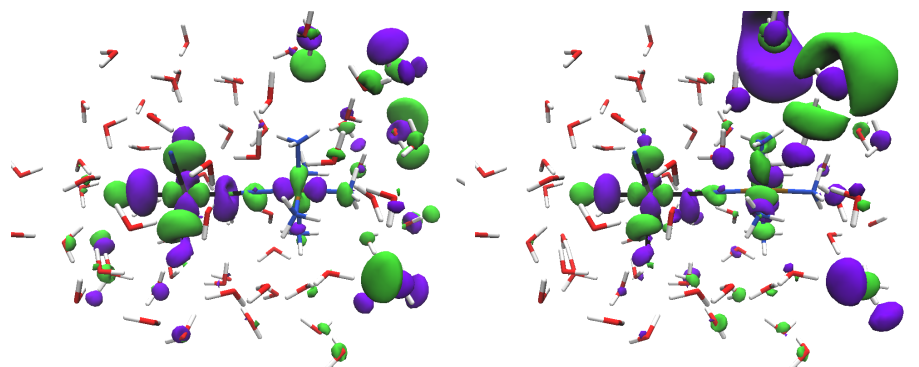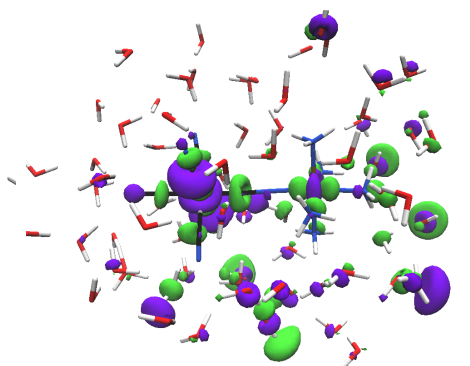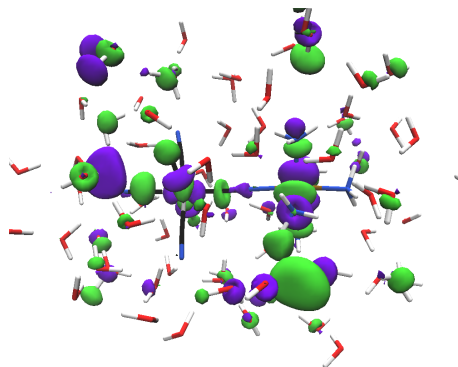
(a) This orbital has a 20% contribution.
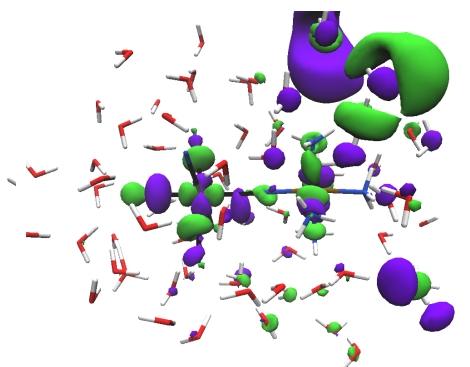
(b) This orbital has a 9% contribution.
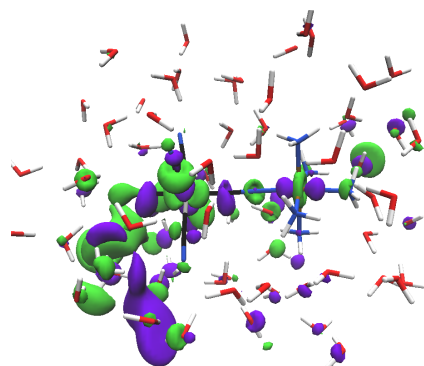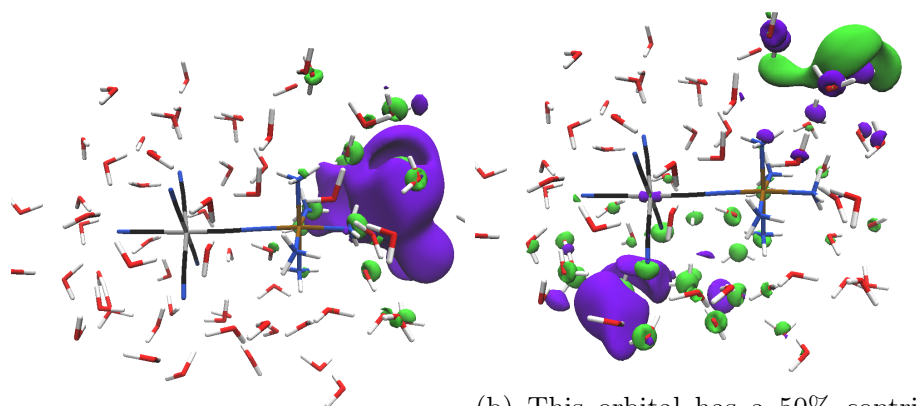
(c) This orbital has a 16% contribution.
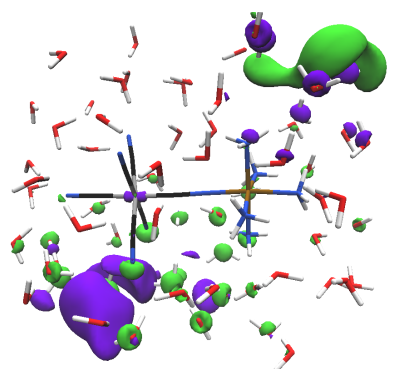
(d) This orbital has a 15% contribution.
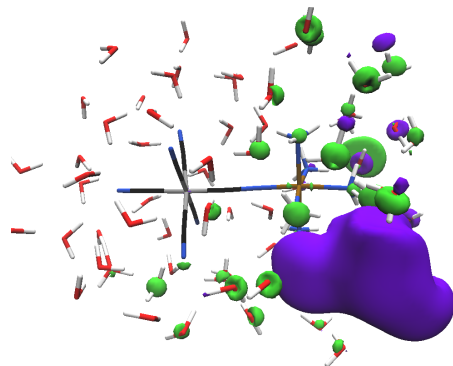
(e) This orbital has a 9% contribution.

Figure S17: **B peak molecular orbitals.** Molecular orbitals associated with the B peak, calculated at an Fe hole charge of 0.68.
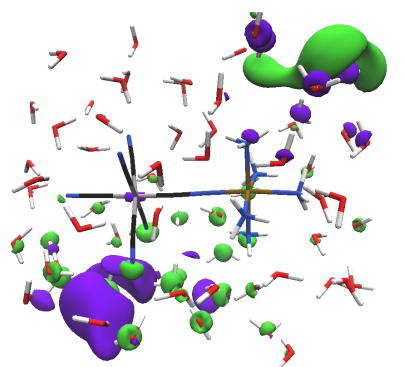
(a) This orbital has a 98% contribution to the C1 peak.

(b) This orbital has a 50% contribution to the C2 peak and a 25% contribution to the C3 peak.

(c) This orbital has a 23% contribution to the C2 peak and a 69% contribution to the C3 peak.

(d) This orbital has a 10% contribution to the C2 peak.

Figure S18: **C peak molecular orbitals.** Molecular orbitals associated with the C peaks, calculated at an Fe hole charge of 0.68.

spectra. The width, and relative amplitude of the excited state peaks are given by the APS HERFD-XANES measurement of ($[Fe^{III}(CN)_6]^{3-}$) measured at the ($[Fe^{II}(CN)_6]^{4-}$) Kα_1 peak emission energy. This is critical since the excited state FeRu HERFD-XANES spectra is also taken at the FeRu ground state Kα_1 emission energy, and the HERFD-XANES spectra, especially the C peak amplitude, varies slightly when taken at different emission energies. A careful examination of this effect is shown in Fig. S13 of the Supplementary Information. We then fit the position of the excited state peaks, the position of the exited state Fe K-edge, and a scaling factor to the excited state peaks amplitudes to account for changes in the overall absorption between the two molecules. We purposely do not fit the individual amplitude of each peak because we expect that the relative peak amplitudes should remain relatively constant, given that the relative peak amplitudes only vary by 0.7% between ($[Fe^{II}(CN)_6]^{4-}$) and FeRu. This reduction in dimensionality allows us to converge on a final reconstruction. The total amplitude of the difference signal is set by the excitation fraction.

3.8   HERFD-XANES fit parameters

The HERFD-XANES fit parameters used to determine the peak positions used in Fig. 6 of the main text are shown in Tables S18 and S18 along with the corresponding fit equation. For completeness, Eq. 8 is the equation for a HERFD-XANES spectra with three peaks. For spectra with only two peaks, the amplitude of the A peak is set to zero.

$$
\begin{aligned}
F(x) =& A_A * e^{-(x-x_{0,A})^2/\sigma_A} + A_B * e^{-(x-x_{0,B})^2/\sigma_B} + A_C * e^{-(x-x_{0,C})^2/\sigma_C} \\
& + F_0 + A_{edge} * \mathrm{erf}((x - x_{0,edge})/\psi_{edge})
\end{aligned}
\tag{8}
$$

3.9   Additional calculated XANES spectra

Additional calculated XANES spectra are shown in Fig. S19 for the other hole densities from trajectory 2 in Fig. 6 of the main text. Given the size of the C peak, we also consider three

Table S18: **HERFD-XANES fit parameters.** Fit parameters of FeRu are shown here.

Parameter	Value
FeRu excited state measured at LCLS	
$x_{0,A}$	7113.3 eV
$x_{0,B}$	7115.8 eV
$x_{0,C}$	7119.5 eV
x_{edge}	7121.6 eV
B and C peak scale factor	0.76
FeRu ground state measured at LCLS	
σ_B	0.50 eV^2
A_B	389.3
$x_{0,B}$	7114.4 eV
σ_C	1.89 eV^2
A_C	932.7
$x_{0,C}$	7117.1 eV
F_0	1581
A_{edge}	953.4
ψ_{edge}	3.14 eV
$x_{0,edge}$	7119.1 eV
FeRu ground state measured at APS	
σ_B	0.14 eV^2
A_B	246.5
$x_{0,B}$	7114.2 eV
σ_C	1.71 eV^2
A_C	729.2
$x_{0,C}$	7117.2 eV
F_0	1927
A_{edge}	1960
ψ_{edge}	7.92 eV
$x_{0,edge}$	7122.9 eV

transitions associated the the C peak, highlighted with vertical arrows. As discussed in the main text, the calculated XANES spectra does not accurately predict the position of the C peak. Therefore, rather than using the broadened C peak, we examine how individual transitions blue shift with Fe hole charge. In Fig. S22 we show that the C peak transitions tend to move together with the hole charge, and therefore the trend between B, C peak energy splitting and Fe hole charge is likely insensitive to our exact selection of C peak transition. We therefore use the three C peak transitions highlighted in Fig. S19 to calculate

Table S18: **HERFD-XANES fit parameters continued.** Fit parameters of ($[Fe^{III}(CN)_6]^{3-}$) and ($[Fe^{II}(CN)_6]^{4-}$) are shown here.

Parameter	Value
($[Fe^{III}(CN)_6]^{3-}$) ground state measured at APS	
σ_A	0.27 eV^2
A_A	560.4
$x_{0,A}$	7113.5 eV
σ_B	0.87 eV^2
A_B	565.0
$x_{0,B}$	7114.6 eV
σ_C	1.98 eV^2
A_C	1790
$x_{0,C}$	7118.7 eV
F_0	1927
A_{edge}	2092
ψ_{edge}	3.60 eV
$x_{0,edge}$	7120.9 eV
($[Fe^{II}(CN)_6]^{4-}$) ground state measured at APS	
σ_B	0.16 eV^2
A_B	542.5
$x_{0,B}$	7114.1 eV
σ_C	1.2 eV^2
A_C	1602
$x_{0,C}$	7116.9 eV
F_0	3033
A_{edge}	3113
ψ_{edge}	6.73 eV
$x_{0,edge}$	7120.7 eV

the B, C peak energy splitting. We account for the ground state shift between the calculated and experimental B, C peak splitting by subtracting this difference from the ground state calculated B, C peak splitting in the lower right panel of Fig. S19 and the lower panel of Fig. S21. We also note that as the hole charge changes, transitions of different symmetry can change position in energy in the C peak region. Figure S19 shows how the C3 and C2 peak, identified by their symmetry, change position. The transition densities for each of these peaks is shown in Fig. S20.

Similar to the calculated A, B peak splitting, the B, C peak splitting also shifts linearly with the Fe hole charge.
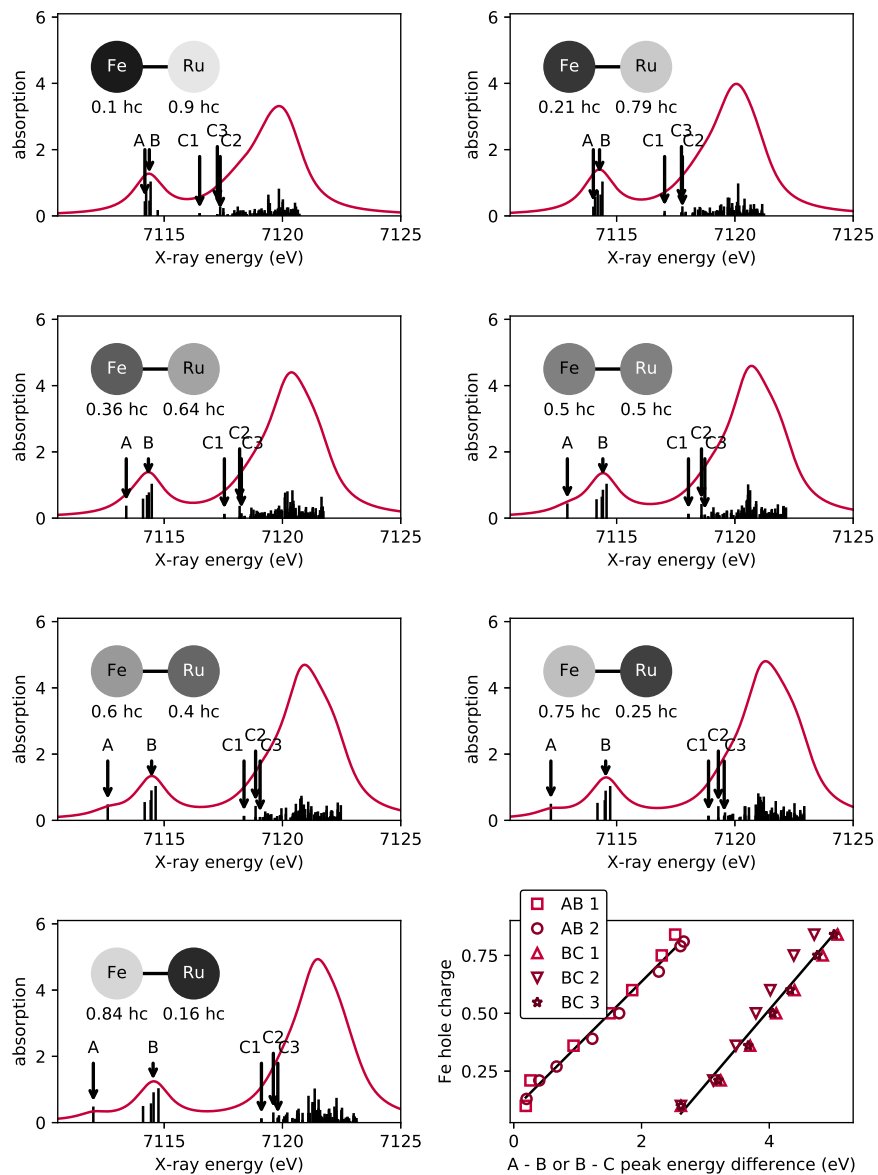
Figure S19: **Calculated absorption spectra.** The calculated absorption spectra for each of the hole densities shown in trajectory 2 in Fig. 6 are shown here. We note that the C2 and C3 peak to swap places in energy after a hole charge of 0.21 on the Fe atom.
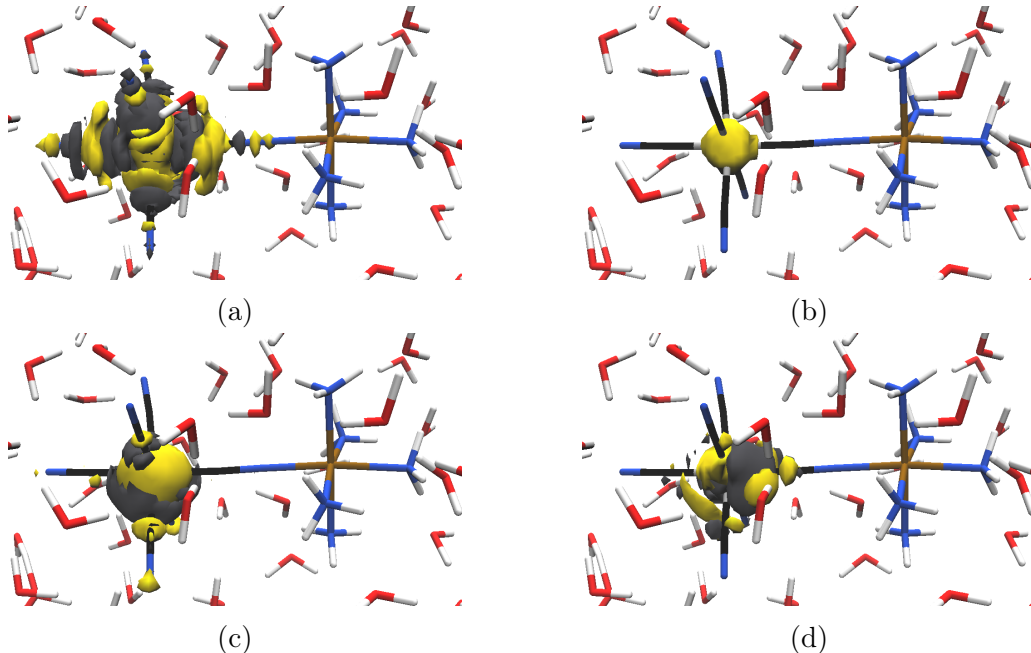
Figure S20: **Calculated B and C transition density plots.** The negative density is grey while the positive density is yellow. (a) B peak transition for a 0.6 Fe hole charge. (b) C1 peak transition for a 0.6 Fe hole charge. (c) C2 peak transition for 0.6 Fe hole charge. (d) C2 peak transition for 0.6 Fe hole charge.

3.10   Measured Fe hole charge from B and C peak energy difference

In Fig. S19, we see that like the A, B peak splitting, the calculated B, C peak energy splitting also shifts linearly with the Fe hole charge. Given the size of the C peak compared to the A peak, it is possible that the C peak could be used to determine the Fe hole charge with a greater signal to noise. Therefore, we show the same analysis for the B, C peak splitting in Fig. S21 as in Fig. 6 from the main text using the C peak transitions highlighted in Fig. S19. We find that the measured Fe hole charge from the B and C peaks is 0.47 ± 0.21, which does not overlap with our Fe hole charge calculation from the A and B peaks. Given that the calculation was not able to accurately predict the ground state B-C splitting, it is possible that the calculation is also under predicting the extent that the B-C peak splitting is changing with Fe hole charge. However, future experimental and theoretical measurements could provide better predictions of the C peak, which given the signal size of the C peak shift, could provide a more accurate measurement of the Fe hole charge.
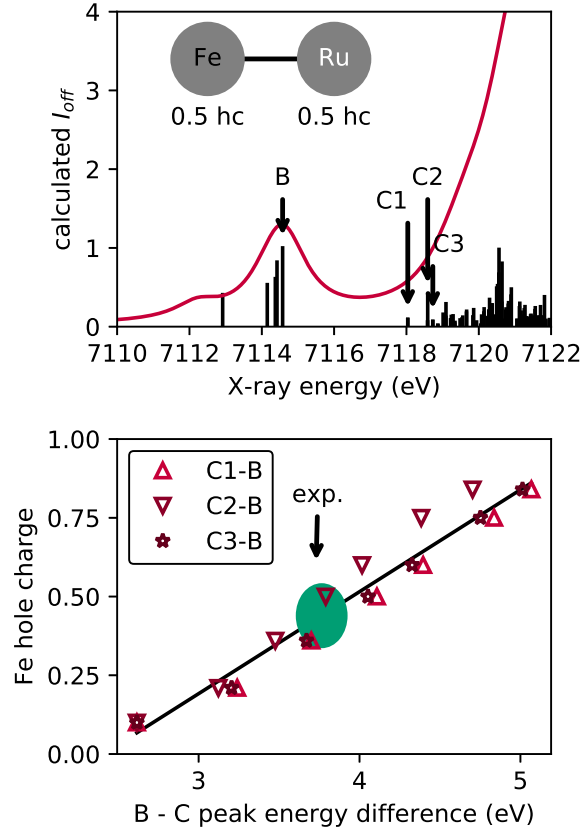
Figure S21: **Calculated and measured hole charge from the B and C peak.** The lower panel shows the calculated Fe hole charge as a function of the B-C peak splitting. The corresponding experimental measurement is shown as the green oval with the uncertainty given by its size. In the upper panel, the calculated spectra is shown for the Fe hole densities for an Fe hole charge of 0.5. The arrows indicate which roots were chosen to represent each B and C peak.

3.11   Calculated C peak transitions

To asses how sensitive the calculated B-C peak splitting is to our choice of the C peak transition line we show how each transition in the C peak region shifts with the Fe hole charge. We see that the C peak transitions all generally move together, increasing nearly linearly with the Fe hole charge. This trend indicates that the calculated B-C peak splitting is relatively insensitive to the C peak choice.
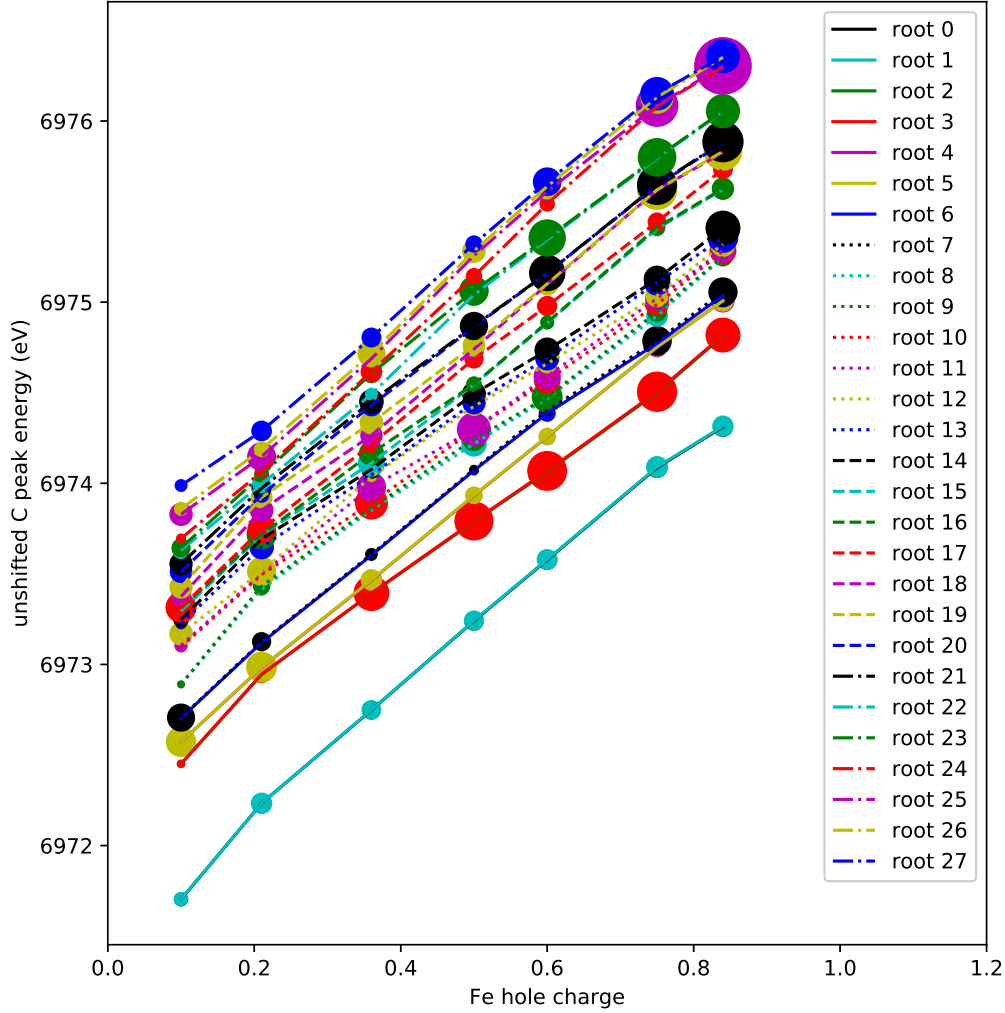
Figure S22: **Transitions in the C peak.** The energy of the first 27 roots in the calculated C peak region are shown as a function of the Fe hole charge. Each transition is plotted as a function of the Fe hole charge and labeled by its root number. The intensity of each transition is indicated by the size of each data point. We note that some roots are closely overlapped in energy, such as root 0 and root 1, making them difficult to distinguish from each other on this plot. We make the data points semi-transparent to assist in this identification.

References

(1) Biasin, E. et al. *Accepted for publication in Nature Chemistry*

(2) James, G.; Witten, D.; Hastie, T.; Tibshirani, R. *An Introduction to Statistical Learning*; Springer Texts in Statistics; Springer New York: New York, NY, 2013; Vol. 103.